Monthly Notices
of the
ROYAL ASTRONOMICAL SOCIETY

MNRAS **460,** 2157–2179 (2016)
Advance Access publication 2016 May 5

doi:10.1093/mnras/stw1066

Bimodality of low-redshift circumgalactic O VI in non-equilibrium EAGLE zoom simulations

Benjamin D. Oppenheimer,[1⋆] Robert A. Crain,[2] Joop Schaye,[3] Alireza Rahmati,[4] Alexander J. Richings,[5] James W. Trayford,[6] Jason Tumlinson,[7] Richard G. Bower,[6] Matthieu Schaller[6] and Tom Theuns[6]

[1]*CASA, Department of Astrophysical and Planetary Sciences, University of Colorado, 389 UCB, Boulder, CO 80309, USA*
[2]*Astrophysics Research Institute, Liverpool John Moores University, 146 Brownlow Hill, Liverpool L3 5RF, UK*
[3]*Leiden Observatory, Leiden University, PO Box 9513, NL-2300 RA Leiden, the Netherlands*
[4]*Institute for Computational Science, University of Zürich, Winterthurerstrasse 190, CH-8057 Zürich, Switzerland*
[5]*Department of Physics and Astronomy and CIERA, Northwestern University, 2145 Sheridan Road, Evanston, IL 60208, USA*
[6]*Institute for Computational Cosmology, Durham University, South Road, Durham DH1 3LE, UK*
[7]*Space Telescope Science Institute, 3700 San Martin Drive, Baltimore, MD 21218, USA*

Accepted 2016 May 3. Received 2016 April 25; in original form 2016 March 3

ABSTRACT

We introduce a series of 20 cosmological hydrodynamical simulations of L^* ($M_{200} = 10^{11.7}$–$10^{12.3}\,M_\odot$) and group-sized ($M_{200} = 10^{12.7}$–$10^{13.3}\,M_\odot$) haloes run with the model used for the EAGLE project, which additionally includes a non-equilibrium ionization and cooling module that follows 136 ions. The simulations reproduce the observed correlation, revealed by COS-Halos at $z \sim 0.2$, between O VI column density at impact parameters $b < 150$ kpc and the specific star formation rate (sSFR $\equiv$ SFR/M_*) of the central galaxy at $z \sim 0.2$. We find that the column density of circumgalactic O VI is maximal in the haloes associated with L^* galaxies, because their virial temperatures are close to the temperature at which the ionization fraction of O VI peaks ($T \sim 10^{5.5}$ K). The higher virial temperature of group haloes ($>10^6$ K) promotes oxygen to higher ionization states, suppressing the O VI column density. The observed $N_{\rm O\,VI}$–sSFR correlation therefore does not imply a causal link, but reflects the changing characteristic ionization state of oxygen as halo mass is increased. In spite of the mass dependence of the oxygen ionization state, the most abundant circumgalactic oxygen ion in both L^* and group haloes is O VII; O VI accounts for only 0.1 per cent of the oxygen in group haloes and 0.9–1.3 per cent with L^* haloes. Nonetheless, the metals traced by O VI absorbers represent a fossil record of the feedback history of galaxies over a Hubble time; their characteristic epoch of ejection corresponds to $z > 1$ and much of the ejected metal mass resides beyond the virial radius of galaxies. For both L^* and group galaxies, more of the oxygen produced and released by stars in the circumgalactic medium (within twice the virial radius) than in the stars and interstellar medium of the galaxy.

Key words: methods: numerical – galaxies: formation – galaxies: haloes – intergalactic medium – quasars: absorption lines – cosmology: theory.

1 INTRODUCTION

A self-consistent model of galaxy formation requires an understanding of the relationship between the galactic components, stars and the interstellar medium (ISM), and the surrounding gaseous reservoir that extends to the virial radius and beyond, defined roughly as the circumgalactic medium (CGM). At redshift $z < 0.5$, the galactic component is well characterized through observational inference of stellar masses, star formation rates (SFRs), and morphologies. The corresponding CGM remains much more challenging to characterize, because its diffuse nature generally requires absorption line spectroscopy towards background ultraviolet (UV)-bright sources. This significant reservoir of halo gas clearly plays a central role in the cycling of baryons into and out of a galaxy, regulating its growth; however, the details of the galaxy–CGM relationship remain elusive.

Until recently, UV absorption line spectroscopy could not target low-redshift galactic haloes, because only a small number of quasars were bright enough. The study of the metal enrichment of

⋆ E-mail: benjamin.oppenheimer@colorado.edu

the low-z intergalactic medium (IGM) relied on surveys of metal lines in serendipitous sight lines providing a cross-section-weighted sampling (e.g. Thom & Chen 2008; Tripp et al. 2008; Wakker & Savage 2009; Tilton et al. 2012; Danforth et al. 2016). These observations could be confronted with cosmological hydrodynamical simulations that included metal enrichment from galactic superwinds to learn how the nucleosynthetic products of star formation enrich the diffuse CGM and IGM (e.g. Aguirre et al. 2001; Schaye et al. 2003; Springel & Hernquist 2003b; Oppenheimer & Davé 2006, 2009; Tornatore et al. 2010; Wiersma et al. 2010; Cen & Chisari 2011; Smith et al. 2011; Tepper-Garcia et al. 2011; Tescari et al. 2011; Oppenheimer et al. 2012; Crain et al. 2013; Rahmati et al. 2016).

The installation of the Cosmic Origins Spectrograph (COS) greatly increased the throughput of UV spectroscopy on the *Hubble Space Telescope* (*HST*) platform (e.g. Savage et al. 2010), enabling the use of fainter quasar targets illuminating foreground galactic haloes. Several *HST* programs have exploited this new capability to investigate the gaseous environments of a sample of low-z haloes, including COS-Halos (Tumlinson et al. 2013), COS-Dwarfs (Bordoloi et al. 2014), and COS-GASS (Borthakur et al. 2015). Other recent studies have also characterized the CGM relative to samples of galaxies, including Chen et al. (2010), Bordoloi et al. (2011), Kacprzak et al. (2011, 2015), Borthakur et al. (2013), Churchill et al. (2013), Nielsen, Churchill & Kacprzak (2013), Stocke et al. (2013), Liang & Chen (2014) at low-z and Turner et al. (2014) at high-z.

One of the first COS-Halos results demonstrated statistically that the properties of O VI absorption, out to impact parameter b = 150 kpc, correlate with the properties of the host galaxies (Tumlinson et al. 2011, hereafter T11). The strongest correlation was found between the O VI column density ($N_{\rm O\,VI}$) and the specific star formation rate (sSFR $\equiv$ SFR/M_*) of the galaxy, such that the bimodality in sSFR between the COS-Halos star-forming sample and the passive sample is clearly reflected in their O VI columns. Of the 12 COS-Halos passive galaxies, defined as having sSFR less than 10^{-11} yr^{-1}, at least half have $N_{\rm O\,VI} < 10^{14.0}$ cm^{-2}, while 90 per cent of the 30 COS-Halos star-forming galaxies have $N_{\rm O\,VI} > 10^{14.2}$ cm^{-2} and the median $N_{\rm O\,VI}$ is $10^{14.5}$ cm^{-2} at $b < 150$ kpc.

T11 identified O VI haloes as a major reservoir of the metals synthesized by star-forming galaxies, estimating a typical O VI mass of $\approx 2 \times 10^6$ M$_\odot$ when summing the median O VI column of $10^{14.5}$ cm^{-2} over a 150 kpc radius aperture. The total mass of oxygen traced by COS-Halos is at least 1.2×10^7 M$_\odot$ when assuming a maximum O VI ionization fraction, $x_{\rm O\,VI} = 0.2$. Peeples et al. (2014) explored the O VI haloes in the context of the total metal budget estimated to be synthesized by galaxies, concluding that there exists nearly as much metal mass traced by circumgalactic O VI as in the ISM of galaxies with $M_* < 10^{10}$ M$_\odot$ for $x_{\rm O\,VI} = 0.2$.

The discovery of such a large reservoir of O VI-traced metals extending far beyond the stellar disc of the galaxy leads to several questions about the dynamical link between galaxies and their associated CGM. Is there a direct relation between the O VI in haloes and star formation as suggested by the O VI–sSFR correlation? Such a link would imply that typical L^* galaxies are spewing enriched gas in galactic winds out to 150 kpc and beyond in the low-z Universe. A number of large-volume simulations (e.g. Ford et al. 2013, 2016; Suresh et al. 2015a,b) and zooms with cosmological initial conditions (e.g. Stinson et al. 2012; Hummels et al. 2013; Shen et al. 2014; Gutcke et al. 2016) have found an intimate link between galaxies and their metal-enriched CGM. Simulations that specifically compared with the COS-Halos survey find lower O VI column densities than observed around star-forming galaxies (Suresh et al. 2015b; Ford et al. 2016). The Ford et al. (2016) simulations do not include active galactic nucleus (AGN) feedback and do not reproduce the O VI bimodality, while Suresh et al. (2015b) argue that AGN feedback clears out the CGM around passive galaxies thus reducing O VI column densities around passive galaxies.

Another possibility is that CGM O VI is not directly attributable to recent star formation or AGN activity, and that instead the O VI bimodality arises from a more fundamental relationship. To assess this possibility, we need to ask what is the physical nature of O VI? If O VI is predominantly photoionized gas at $\sim 10^4$ K (e.g. Oppenheimer & Davé 2009), then such absorbers could be a signature of cold flows (e.g. Kereš et al. 2005; Dekel et al. 2009; van de Voort et al. 2012) feeding star formation, which may subside around passive galaxies. Enhanced photoionization from young stars could also ionize O VI around star-forming galaxies (Oppenheimer & Schaye 2013b; Vasiliev, Ryabova & Shchekinov 2015; Suresh et al. 2015b). Oppenheimer et al. (2012) demonstrated that increasing the ionization background strength at the O VI ionization potential can result in photoionized O VI tracing higher densities, even in circumgalactic halo gas. Alternatively, if O VI is primarily collisionally ionized at its $10^{5.5}$ K peak (e.g. Heckman et al. 2002; Cen & Chisari 2011; Smith et al. 2011; Tepper-Garcia et al. 2011; Faerman, Sternberg & McKee 2016), then it signals a hot halo component apparently associated with star-forming galaxies. Is this warm-hot component related to recent outflows or does it trace the temperature of a virialized, quasi-static halo? If the latter, do passive galaxies lack O VI haloes, because their virial temperatures are much hotter than $10^{5.5}$ K?

Knowledge of the physical cause of the ionization is required to constrain $x_{\rm O\,VI}$, from which the total mass of oxygen and metals in the CGM is inferred. Because the O VI-traced CGM mass scales inversely with $x_{\rm O\,VI}$, far more CGM oxygen would be present if $x_{\rm O\,VI}$ is much lower than the maximal value implied by ionization analyses. Hence, it is uncertain how much underlying CGM oxygen the COS-Halos O VI observation indicate.

To understand the origin and nature of O VI in a set of haloes hosting galaxies corresponding to those probed by COS-Halos, we need cosmological simulations that can simultaneously model the stellar build-up of galaxies, the feedback processes that eject gas from galaxies, and the detailed atomic processes that govern the abundances of the ions observed in the CGM. Here, we run a series of zoom simulations targeting a range of galactic haloes similar to those probed by the COS-Halos survey using the same model as the EAGLE simulations (Crain et al. 2015; Schaye et al. 2015, hereafter S15). The parameters of the subgrid physics routines employed by the EAGLE simulations were calibrated to reproduce the observed $z \sim 0.1$ galactic stellar mass function, the supermassive black hole (SMBH) mass–M_* relation, and the sizes of galaxy discs using a combination of star formation (SF)-driven thermal winds and SMBH thermal winds. Observations of the CGM were not used to calibrate the EAGLE simulations, therefore, the outcomes here are genuine predictions of the model.

Here we integrate the non-equilibrium (NEQ) ionization and dynamical cooling module introduced by Oppenheimer & Schaye (2013a, hereafter OS13) into the EAGLE simulation code to trace the evolution of 136 ions of 11 elements on the fly, which we activate at late times for evolved haloes. The module includes photoionization from a slowly evolving meta-galactic background, in this case the Haardt & Madau (2001) quasar+galaxy background. We also note that this work is the first we know of to integrate ion-by-ion cooling rates including for the metals (Gnat & Ferland 2012; OS13) into a

cosmological simulation. NEQ ionization of oxygen was explored in simulations by Cen & Fang (2006) and Yoshikawa & Sasaki (2006), but they did not perform dynamical cooling. We discuss the NEQ effects in Appendix A, but note that these do not significantly affect the O VI columns when using a uniform meta-galactic background, nor do they alter the integrated properties of galaxies (M_*, SFR, colour).

Our investigation focuses on the O VI column density observations from COS-Halos. We stress that the EAGLE feedback model has not been calibrated to reproduce the properties of the CGM. Nevertheless, EAGLE shows agreement with cosmic H I statistics tracing the IGM over a Hubble time (Rahmati et al. 2015). Furthermore, because EAGLE reproduces key stellar and cold ISM properties of galaxies (e.g. Furlong et al. 2015a,b; Lagos et al. 2015, 2016; S15; Trayford et al. 2015; Segers et al. 2016; Bahé et al. 2016), while explicitly following the hydrodynamics, it is an ideal testbed for this study and will indicate whether additional physical processes are necessary to reproduce CGM measurements. This enables us to consider the total metal budget inside and beyond galaxies as done by Bouché et al. (2007), Zahid et al. (2012), and Peeples et al. (2014). We also compare our results to the related work of Rahmati et al. (2016), who explored IGM metal-line statistics, including O VI, in the EAGLE cosmological boxes. Throughout we use the EAGLE-RECAL prescription for all zooms as discussed in S2; however, it should be noted that the main EAGLE cosmological boxes use two different prescriptions (REF and RECAL) at two different resolutions, which we discuss in Appendix B and show that there is not a significant difference for our main results.

The layout of the paper is as follows. We describe our zoom simulations and implementation of our NEQ module in Section 2. We present the physical nature and origin of the oxygen-traced CGM in Section 3, and then confront the COS-Halos observations in Section 4. The global content of oxygen produced and distributed by galaxies is considered in Section 5. We discuss the implications of our results in Section 6 and summarize in Section 7. NEQ effects and resolution convergence are explored in the appendices.

2 SIMULATIONS

In this section, we give a brief overview of the EAGLE simulation code, followed by how our NEQ module is integrated with it. We then describe our zoom simulations with attention paid to how the adopted physical model used here differs from the standard EAGLE implementation.

2.1 The EAGLE simulation code

The EAGLE simulation code is an extensively modified version of the *N*-body+smoothed particle hydrodynamic (SPH) code GADGET-3 last described by Springel (2005), which is described in detail by S15. The main modifications to the entropy-conserving SPH implementation of the GADGET-3 code (Springel & Hernquist 2003a) comprise (i) the pressure–entropy SPH formulation described by Hopkins (2013), (ii) the artificial viscosity switch of Cullen & Dehnen (2010), (iii) the artificial conduction switch of Price (2008), (iv) the time step limiter from Durier & Dalla Vecchia (2012) to improve energy conservation during sudden changes of internal energy, and (v) a C2 Wendland (1995) 58-neighbour kernel to suppress particle-pairing instabilities (Dehnen & Aly 2012). Collectively, these updates are referred to as 'Anarchy' (Dalla Vecchia, in preparation; see also appendix A of S15) and the impact of their inclusion on the galaxy population was explored by Schaller et al. (2015).

A number of subgrid physics modules are included in the EAGLE code. Equilibrium radiative cooling and photoheating rates are computed for 11 elements exposed to the Haardt & Madau (2001) extragalactic ionization background plus the cosmic background radiation as described by Wiersma, Schaye & Smith (2009a). These rates are computed using CLOUDY (version 07.02; Ferland et al. 1998), and are replaced here with the NEQ rates of OS13 described in Section 2.2 when run in NEQ mode.

Star formation is modelled using the Schaye & Dalla Vecchia (2008) pressure-based law. A pressure floor, $P_{\rm EOS} \propto \rho^{4/3}$ is additionally imposed, corresponding to a polytropic equation of state, normalized to $T_{\rm EOS} = 8000$ K at $n_{\rm H} = 0.1$ cm^{-3}, because we do not resolve the Jeans scales of the cold ISM. The Kennicutt (1998) SF surface density relationship is reproduced by construction for gas particles above the Schaye (2004) metallicity-dependent SF density threshold. The stellar evolution and enrichment module introduced by Wiersma et al. (2009b) includes element-by-element and mass metal loss from asymptotic giant branch (AGB) stars, stellar winds from massive stars, and supernovae (SNe, core collapse and Type Ia), which is distributed across the SPH kernel of each stellar particle. A Chabrier (2003) initial mass function (IMF) is adopted.

Following Dalla Vecchia & Schaye (2012), feedback associated with star formation and the SMBH growth is implemented by stochastically heating gas particles neighbouring newly formed star particles and accreting SMBH. The energy budgets available associated with stellar feedback and black hole growth govern the probability of heating each SPH particle. Briefly, stellar feedback heats particles by $\Delta T = 10^{7.5}$ K in a single episode 30 Myr after a star particle forms. The fraction of the available energy injected into the ISM depends on the local gas metallicity (Z) to account for more efficient cooling at higher Z, and the local gas density to compensate for artificial radiative losses that occur at high density (see Crain et al. 2015; S15, for further motivation). SMBH growth and AGN feedback are implemented using a single thermal mode following Booth & Schaye (2009) with the addition of the suppression of high angular momentum gas accretion following Rosas-Guevara et al. (2015). We use the high-resolution EAGLE-RECAL prescription, which applies a heating temperature of $\Delta T_{\rm AGN} = 10^{9.0}$ K.

2.2 Non-equilibrium network integrated into EAGLE

The NEQ module, introduced by OS13, explicitly follows the reaction network of 136 ionization states of all 11 elements that contribute significantly to the cooling (H, He, C, N, O, Ne, Si, Mg, S, Ca, and Fe) plus the electron density of the plasma. These are the same elements as are present in the equilibrium cooling module of Wiersma et al. (2009a), enabling a self-consistent switching between using equilibrium lookup tables and the NEQ method. Our reaction network, described fully by OS13, includes radiative and dielectric recombination, collisional ionization, photoionization, Auger ionization, and charge transfer. Cooling is performed ion-by-ion (Gnat & Ferland 2012; OS13) summing over all 136 ions. OS13 verified that this method reproduces published results obtained with other codes. We use particle-based (instead of kernel-smoothed) ion and metal abundances for NEQ ionization and cooling as explained in Section 2.3.3.

Our NEQ module applies the Sundials CVODE[1] solver to integrate the ionization and cooling over a hydrodynamic time step using the backward difference formula and Newton iteration. Although an

[1] https://computation.llnl.gov/casc/sundials/main.html

Table 1. *M5.3* zoom simulation runs.

Name[a]	Resolution[b]	log M^c_{200} (M⊙)	$m^d_{\rm SPH}$ (M⊙)	$m^d_{\rm DM1}$ (M⊙)	ϵ (pc)	log M^c_* (M⊙)	SFR[c] (M⊙ yr^{-1})	$z^e_{\rm NEQ}$	$z^f_{\rm low}$
Gal001	*M5.3*	12.07	2.22e+05	1.19e+06	350	10.27	1.426	0.503	0.0
Gal002	*M5.3*	12.25	2.28e+05	1.22e+06	350	10.26	1.275	0.503	0.0
Gal003	*M5.3*	12.11	2.32e+05	1.24e+06	350	10.25	1.717	0.503	0.0
Gal004	*M5.3*	11.99	2.26e+05	1.21e+06	350	10.08	0.881	0.503	0.0
Gal005	*M5.3*	12.17	2.20e+05	1.18e+06	350	10.40	2.919	0.503	0.0
Gal006	*M5.3*	11.91	2.22e+05	1.19e+06	350	10.08	1.021	0.503	0.0
Gal007	*M5.3*	11.82	2.17e+05	1.16e+06	350	9.93	1.695	0.503	0.0
Gal008	*M5.3*	11.85	2.27e+05	1.22e+06	350	9.95	1.030	0.503	0.0
Gal009	*M5.3*	11.85	2.27e+05	1.22e+06	350	9.94	1.117	0.503	0.0
Gal010	*M5.3*	12.67	2.21e+05	1.19e+06	350	10.67	0.183	0.503	0.0
Grp000	*M5.3*	12.74	2.27e+05	1.22e+06	350	10.70	0.130	0.282	0.0
Grp001	*M5.3*	12.75	2.01e+05	1.08e+06	350	10.65	3.036	0.282	0.205
Grp002	*M5.3*	12.77	2.41e+05	1.29e+06	350	10.79	2.065	0.282	0.0
Grp003	*M5.3*	12.73	2.38e+05	1.28e+06	350	10.76	2.113	0.282	0.0
Grp004	*M5.3*	12.89	2.38e+05	1.28e+06	350	10.74	0.373	0.282	0.0
Grp005	*M5.3*	12.98	2.34e+05	1.25e+06	350	10.75	0.021	0.282	0.149
Grp006	*M5.3*	13.01	2.22e+05	1.19e+06	350	10.57	0.017	0.282	0.0
Grp007	*M5.3*	12.88	2.38e+05	1.28e+06	350	10.60	5.574	0.503	0.0
Grp008	*M5.3*	13.19	2.31e+05	1.24e+06	350	10.95	0.063	0.282	0.205
Grp009	*M5.3*	13.19	2.31e+05	1.24e+06	350	10.90	1.188	0.282	0.0

[a] 'Gal' indicates L^* haloes, 'Grp' indicates group-sized haloes.
[b] $M[\log_{10}(m_{\rm SPH}/{\rm M}_\odot)]$.
[c] At $z = 0.205$.
[d] SPH and DM1 particle masses vary slightly between different zoom initial conditions.
[e] $z_{\rm NEQ}$ is the redshift when the NEQ ionization and cooling are turned on.
[f] $z_{\rm low}$ is the redshift to which the NEQ simulations are run.

extended version of the network is also capable of modelling ISM chemistry including molecular formation, cooling, and dissociation (see Richings, Schaye & Oppenheimer 2014), we focus on the CGM and do not use the NEQ network for gas densities above the metallicity-dependent SF threshold. For ISM gas, defined as having non-zero SFR, we use equilibrium lookup tables tabulated as functions of density assuming $T = 10^4$ K, although we note that this matters little as the ion abundances will rapidly evolve when the SPH particle is heated by feedback, and the NEQ network followed. Upon enrichment, SPH particles receive the new metals in their ground-state ions. The vast majority of enrichment occurs in the ISM gas, where the network is not used. However, enrichment of gas followed using the NEQ network occurs when stars outside of galaxies enrich via delayed feedback (e.g. Type Ia SNe and AGB winds). Our exploration here focuses on CGM gas traced by oxygen absorption, most of which is far from galaxies; hence the details of the ion abundances in ISM gas and from recent enrichment is essentially inconsequential. We set the CVODE absolute tolerance to 10^{-9} and the relative tolerances to 10^{-3}. We do not use a self-shielding prescription for dense gas in either equilibrium or NEQ.

2.3 Zoom simulations

2.3.1 Initial conditions

We assume the same Planck Collaboration I (2014) cosmological parameters adopted by the EAGLE simulations: $\Omega_{\rm m} = 0.307$, $\Omega_\Lambda = 0.693$, $\Omega_{\rm b} = 0.04825$, $H_0 = 67.77$ km s^{-1} Mpc^{-1}, $\sigma_8 = 0.8288$, and $n_{\rm s} = 0.9611$. To generate the zoomed initial conditions, we use initial conditions generated using the second-order Lagrangian perturbation theory method of Jenkins (2010) and the public Gaussian white noise field PANPHASIA (Jenkins & Booth 2013). Targets for resimulation are identified at $z = 0$, and the particles comprising a spherical region that encloses the target object to a radius of $3R_{200}$ (where R_{200} encloses an overdensity of 200× the critical overdensity) are traced back to their coordinates in the unperturbed initial particle distribution. A contiguous surface enclosing the particles is identified out to 3× the virial radius, and the volume it encloses is resampled with a high-resolution particle load realized by tiling a cubic periodic glass distribution (White 1994). This high-resolution particle load is divided into SPH and high-resolution dark matter (DM1) particles, using $\Omega_{\rm b} = 0.04825$ and $\Omega_{\rm m} - \Omega_{\rm b} = 0.259$, respectively. The remaining volume within the simulation domain is resampled with an undivided load of collisionless particles whose resolution decreases as a function of distance from the surface ensuring the faithful reproduction of large-scale gravitational forces throughout the high-resolution region. A glass-like particle distribution guarantees that the initial particle load is essentially free of unwanted power above shot noise frequency. The high-frequency components of the Gaussian random field perturbations can then faithfully be imposed on the zoom region. The initial conditions are generated at $z = 127$.

2.3.2 Selected haloes

We simulate two sets of haloes, a sample of 10 L^* haloes selected from the EAGLE RECAL-L025N0752 simulation, and a sample of 10 'group-sized', super-L^* haloes from the REF-L100N1504 simulation. The L^* galaxy haloes are referred to as Gal001–Gal010 and the group haloes are referred to as Grp000–Grp009 in Table 1. We run at three resolutions, which we will refer using the nomenclature $M[\log(m_{\rm SPH}/{\rm M}_\odot)]$, where $m_{\rm SPH}$ is the initial mass of SPH particles.

M5.3 Zooms. We simulate all haloes at our fiducial resolution, corresponding to an SPH particle mass resolution of 2.3×10^5 M⊙, and a DM particle mass of 1.2×10^6 M⊙. The Plummer-equivalent softening length is 350 proper pc below $z = 2.8$, and 1.33 comoving kpc above $z = 2.8$, which corresponds to 1/25th of

the mean interparticle separation. This is the same resolution as achieved by the L025N0752 simulation. We can cross-reference the zoom L^* *M5.3* galaxies with the same galaxies in the L025N0752 galaxies, which we do in Appendix B to ensure that the zooms do not differ substantially from their parent cosmological volume. We also cross-reference the group zooms, although note that these zooms have 8× (2×) higher mass (spatial) resolution than the L100N1504 simulation. All *M5.3* haloes have NEQ runs between the redshift $z_{\rm NEQ}$ and $z_{\rm low}$ as explained in Section 2.3.4, and each has also been run using equilibrium cooling to $z = 0$.

M4.4 Zooms. We simulate the L025N0752 haloes at 8× higher resolution, corresponding to $m_{\rm SPH} = 2.7 \times 10^4\,{\rm M}_\odot$ ($m_{\rm DM} = 1.6 \times 10^5\,{\rm M}_\odot$), and a softening length of 175 proper pc below $z = 2.8$, and 655 comoving pc at earlier times. All of these are run in equilibrium, and a selection in NEQ. We only use these zooms to test resolution convergence in Appendix B and they are listed there in Table B1. These zooms confirm the main CGM results reported throughout; however, their stellar masses are significantly lower, which is why we only use them for resolution convergence tests.

M6.2 Zooms. We simulate a selection of haloes at the resolution of the L100N1504 box, $m_{\rm SPH} = 1.8 \times 10^6\,{\rm M}_\odot$ and $m_{\rm DM} = 9.7 \times 10^6\,{\rm M}_\odot$, and also compare directly to the same galaxies in the 100 Mpc box, which allows us to link our results to the global IGM results of Rahmati et al. (2016), who use this box as their fiducial simulation.

Each zoom is focused on one halo, but surrounding simulated regions often contain additional haloes that are either partially or fully sampled by SPH and high-resolution DM1 particles. We find a set of 'bonus' haloes that we verified to be completely resolved with SPH and DM1 particles out to three times the virial radius (R_{200}), and add these to our sample. Bonus haloes at our main redshift ($z = 0.205$) include three sub-L^* galaxies ($M_{200} \lesssim 10^{11.5}\,{\rm M}_\odot$) found at a distance greater than $3R_{200}$ of the targeted L^* haloes, two low-mass L^* haloes ($M_{200} = 10^{11.6}\,{\rm M}_\odot$) and two L^* haloes ($M_{200} = 10^{12.0\text{–}12.5}\,{\rm M}_\odot$) found beyond $3R_{200}$ of targeted group haloes, and three bonus haloes ($M_{200} = 10^{12.0\text{–}12.6}$) in the Gal010 zoom, which itself is by far the most massive 'Galaxy' zoom, and tracks the formation of a $10^{12.7}\,{\rm M}_\odot$ $z = 0$ halo.

2.3.3 *Running in equilibrium*

We evolve all zooms using the equilibrium cooling rates from Wiersma et al. (2009a) to $z = 0$ using the standard EAGLE code with the only difference being that we do not use kernel-smoothed metallicities to compute cooling rates. As explained by Wiersma et al. (2009b), smoothed metallicities are consistent with the SPH formalism; however, their use when adopting NEQ cooling requires that both particle and smoothed ion abundances are tracked, which for 136 species is a prohibitive memory requirement. Furthermore, smoothing complicates the interpretation of NEQ ionization effects when ion species are averaged over the SPH kernel. Therefore, to enable a consistent comparison of methods, we use particle metallicities in both equilibrium and NEQ runs.

As a consistency test, we run a set of five *M5.3* zoom runs with smoothed metallicities, finding that they have 0.11 dex higher stellar masses than their non-smoothed *M5.3* zoom counterparts. It appears that smoothed metallicities increase the SF efficiencies by distributing metals over more particles, increasing the overall cooling rate of the galaxy, and leading to more star formation. Wiersma et al. (2009b) also showed that in the OWLS simulations, smoothed metallicities increased the SF efficiency. We show in Appendix B that O VI column densities are unaffected by metal smoothing.

2.3.4 *Running in non-equilibrium*

When examining NEQ simulations, we activate the NEQ module at relatively low redshift in order to minimize the computational cost of following 136 ionic species. The magnitude of NEQ effects can be significant in shocks and rapidly cooling gas, and this behaviour is only captured with use of the NEQ module. This module is important to use, in order to recover the correct ion species in all circumstances. It should be noted that we will show that the NEQ effects are generally not important for gas dynamics in a separate study, as predicted by OS13 and also demonstrated by Richings & Schaye (2016). Furthermore, NEQ effects on CGM ion diagnostics (i.e. observables) persist for short times compared to the Hubble timescale, enabling us to begin modelling them only at late times. We discuss the NEQ effects in Appendix A, which are typically small, <0.1 dex for oxygen ions.

The L^* haloes all switch to NEQ cooling at $z_{\rm NEQ} = 0.503$ and the group haloes at $z_{\rm NEQ} = 0.282$. The later NEQ activation for group haloes was adopted to save computational cost. The NEQ runs begin from a snapshot output of the equilibrium run, where we iterate CVODE for a long timescale ($\delta t = 10^6/[n_{\rm H}/{\rm cm}^{-3}]$ yr) for all species to guarantee ionization equilibrium. The EAGLE code then runs as normal with the Wiersma et al. (2009a) cooling replaced by the NEQ module iterating the ionization states and cooling rates via CVODE across the hydrodynamics time step.

For one group zoom (Grp007) we perform two runs, $z_{\rm NEQ} = 0.503$ and 0.282 in order to establish that its properties are not significantly altered at $z = 0.250$, since this is the highest redshift we use to compare to COS-Halos results. We use up to six outputs ($z = 0.250$, 0.205, 0.149, 0.099, 0.053, and 0.0) when confronting COS-Halos measurements to give a greater range of galaxy properties as discussed further in Section 4. Every halo is run past $z = 0.205$, with every *M5.3* L^* halo run to $z = 0$ and 7 out of 10 *M5.3* group haloes run to $z = 0$.

2.3.5 *Basic galaxy properties*

We plot stellar mass and SFR properties of central galaxies in our haloes in Fig. 1 using *M5.3* zooms. We run the SUBFIND algorithm (Springel et al. 2001; Dolag et al. 2009) on our zoom outputs, and quantify halo mass, M_{200}, as the mass within a sphere with mean enclosed density 200× the critical overdensity centred on the galaxy's potential minimum. Galaxy stellar masses (M_*) and SFRs are calculated by summing the appropriate quantities within a 30 physical kpc sphere around the centre of the central subhalo, which almost always hosts the most massive galaxy. The top left-hand panel of Fig. 1 plots the $M_*/(M_{200} \times f_{\rm bar})$ abundance matching relation, where $f_{\rm bar} \equiv \Omega_{\rm b}/\Omega_{\rm m}$, for central galaxies from the six redshifts we examine. While our *M5.3* haloes follow the shape of the relationship recovered by Behroozi, Wechsler & Conroy (2013) and Moster, Naab & White (2013) at $z = 0.2$, they are ∼0.2–0.4 dex lower for $M_{200} \gtrsim 10^{12}\,{\rm M}_\odot$. As discussed earlier, our use of particle metallicities reduces stellar masses by 0.1 dex compared with the smoothed metallicity simulations used to calibrate the feedback efficiencies. Moreover, S15 also find stellar masses 0.2–0.3 dex lower than the abundance matching constraints (Behroozi et al. 2013; Moster et al. 2013) at $M_{200} = 10^{12.0}\,{\rm M}_\odot$ at $z = 0.1$ (RECAL-L025N0752 shown as a thick yellow line with shading for 1σ dispersion).

For each central galaxy at a given redshift, we test whether it would be classified as isolated using criteria similar to those applied by Tumlinson et al. (2013), who select COS-Halos galaxies as being the most luminous galaxy within $b < 300$ kpc of the QSO

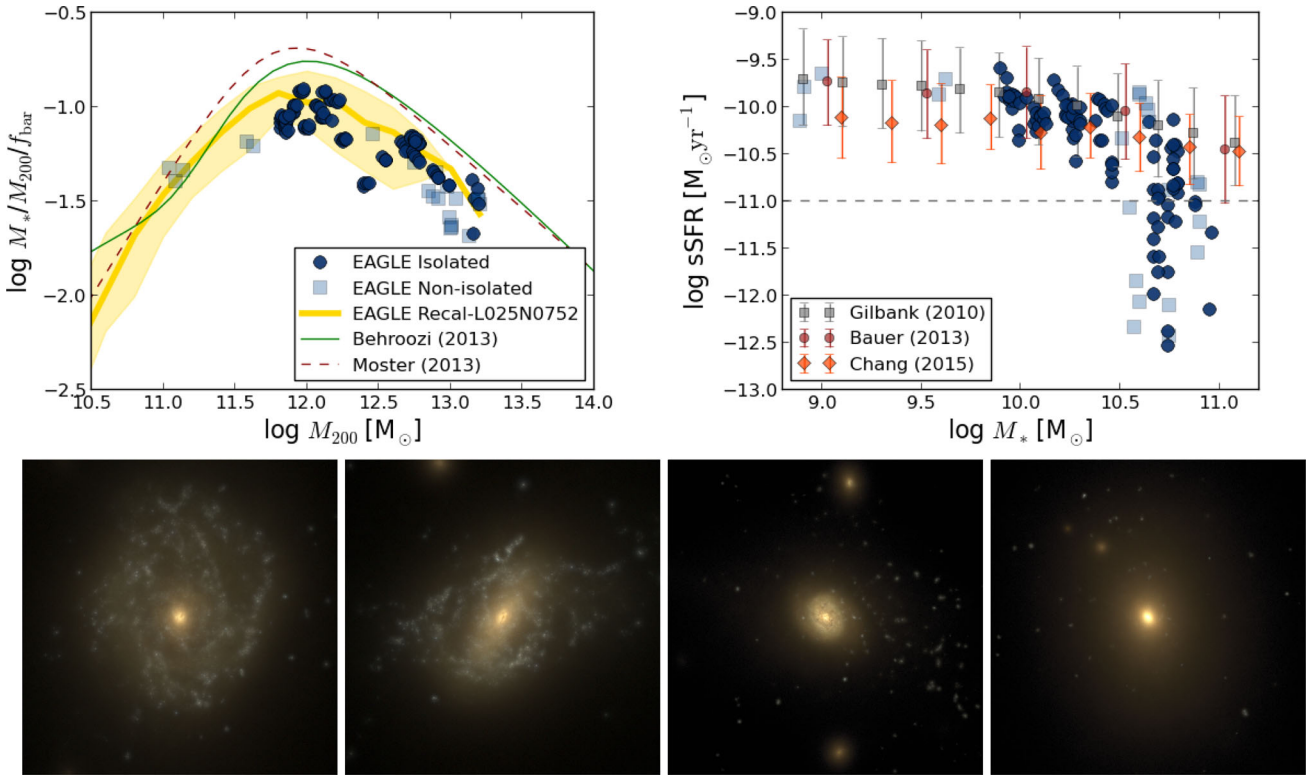

Figure 1. Stellar mass to halo mass ratio plotted as a function of halo mass of zoomed centrals (top left) and sSFR as a function of stellar mass (top right) from six redshifts ($z = 0.25 \rightarrow 0$) that we use in our analysis. Galaxies that can be considered 'isolated' by COS-Halos criteria are indicated by dark circles, while transparent squares indicate galaxies with a neighbouring galaxy with $M_* > 10^{10.3}$ M$_\odot$ within 300 kpc. Three sub-L^* galaxies at $z = 0.205$ are also plotted as light circles. The thick yellow line is the fit to all centrals in the RECAL-L025N0752 simulation (S15) with the shading indicating the 1σ dispersion. Abundance matching results from Behroozi et al. (2013, solid green) and Moster et al. (2013, dashed red) at $z = 0.2$ are displayed on the left, and observations of the sSFR of star-forming galaxies as a function of M_* from Gilbank et al. (2010, grey squares), Bauer et al. (2013, brown circles), and Chang et al. (2015, orange diamonds) are displayed on the right. Bottom panels show simulated 50 kpc SDSS *u*-, *g*-, and *r*-band composite images, including dust, of two star-forming L^* galaxies and two group centrals – a recent merger and a passive galaxy (from left to right). All plots use *M5.3* zooms.

sightline at its redshift. They also note that there are usually no L^* photo-z candidates within 1 Mpc. We use the criterion that there should not be any galaxies with $M_* > 2 \times 10^{10}$ M$_\odot$ within an impact parameter $b = 300$ kpc, first to ensure that our galaxy is the most massive system inside this impact parameter, and secondly because we usually do not simulate surrounding galaxies beyond $3R_{200}$. Often there are surrounding haloes that are not resolved completely by the high-resolution particle load; however, we still use their stellar masses in our isolation criteria to be conservative, although there are only a few cases for which this happens. Dark circles in Fig. 1 indicate haloes that appear isolated in at least one of the three projections we use to cast our sight lines and can be used for comparison with the COS-Halos dataset (see Section 4). Transparent squares are for non-isolated haloes in all three projections, as well as for bonus haloes with $M_{200} < 10^{11.7}$ M$_\odot$, where we only plot their outputs at $z = 0.205$. We include these low-mass haloes for our discussion of halo mass trends in Section 3.1, but not for comparisons to the COS-Halos dataset in Section 4.

We plot the galaxies on the M_*–sSFR plot in the top right-hand panel of Fig. 1 to show that our galaxies follow the general trend of the star-forming sequence observed at low-z by Gilbank et al. (2010), Bauer et al. (2013), and Chang et al. (2015), and a set of massive galaxies in group haloes with low sSFR. Our galaxies do not have a passive clump at sSFR $< 10^{-11}$ yr^{-1} that is as prominent as for the COS-Halos survey, but the EAGLE boxes do reproduce the passive fraction as a function of M_* (S15). Additionally, when we mock COS-Halos surveys in Section 4, the galaxies we select to match the COS-Halos galaxies better reproduce this passive clump. The bottom row of Fig. 1 shows 50 kpc, SDSS *u*-, *g*-, and *r*-band composite maps of two star-forming L^* galaxies (left), and two group centrals, including an active merger and a passive galaxy (right). These maps are generated using the SKIRT radiative transfer code (Baes et al. 2011; Camps & Baes 2015) as described in detail by Trayford et al. (in preparation).

3 PHYSICAL PROPERTIES OF THE OXYGEN-ENRICHED CIRCUMGALACTIC MEDIUM

This section begins by exploring CGM properties across two decades in halo mass, from sub-L^* haloes ($M_{200} \lesssim 10^{11.7}$ M$_\odot$) through L^* haloes ($M_{200} \sim 10^{12}$ M$_\odot$) to group-sized, super-L^* haloes ($M_{200} \gtrsim 10^{12.3}$ M$_\odot$). We further explore the physical trends that establish the ionization structure of the oxygen-enriched CGM. Lastly, we focus on the nature and origin of the O VI that is observed by the COS-Halos survey. Throughout we use *M5.3* zooms.

3.1 Trends with halo mass

We begin our discussion by showing three haloes with masses $M_{200} = 10^{11.1}$, $10^{12.2}$, and $10^{13.2}$ M$_\odot$ in Fig. 2 at the median redshift of the COS-Halos, $z = 0.2$. All images are 600 physical kpc across.

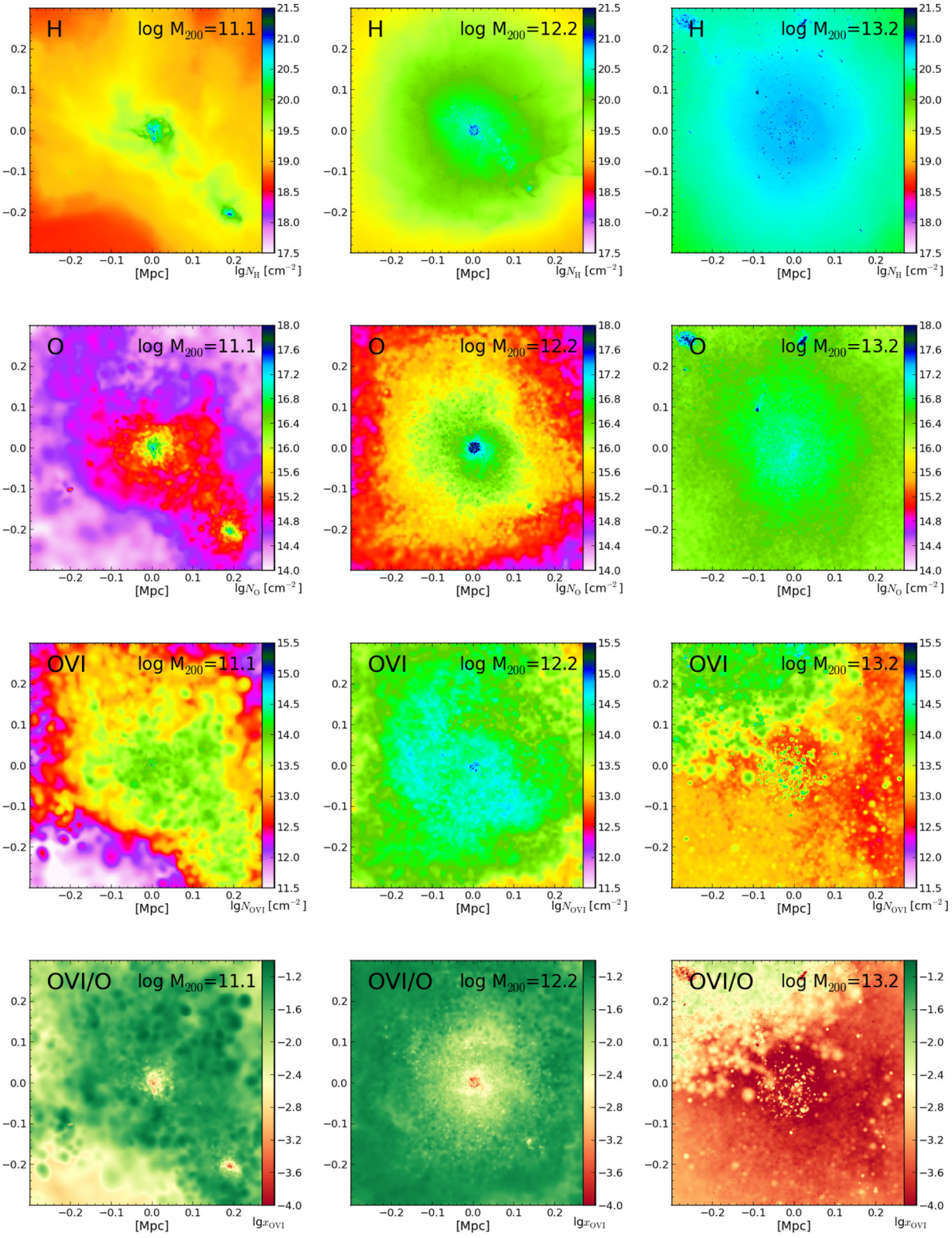

Figure 2. Images of 600 physical kpc on a side $z = 0.205$ snapshots of three haloes with mass $10^{11.1}$, $10^{12.2}$, and $10^{13.2}\,M_{\odot}$ representative of sub-L^*, L^*, and group-sized haloes, respectively, from left to right. The top row shows hydrogen columns. The second row shows oxygen columns, while the third row shows O VI columns. The bottom row shows maps of the O VI fraction. The selected galaxies are a bonus sub-L^* central galaxy in the Gal005 zoom, the main L^* galaxy in the Gal005 zoom, and the super-L^* galaxy in the Grp008 zoom. Projections are 2400 kpc deep.

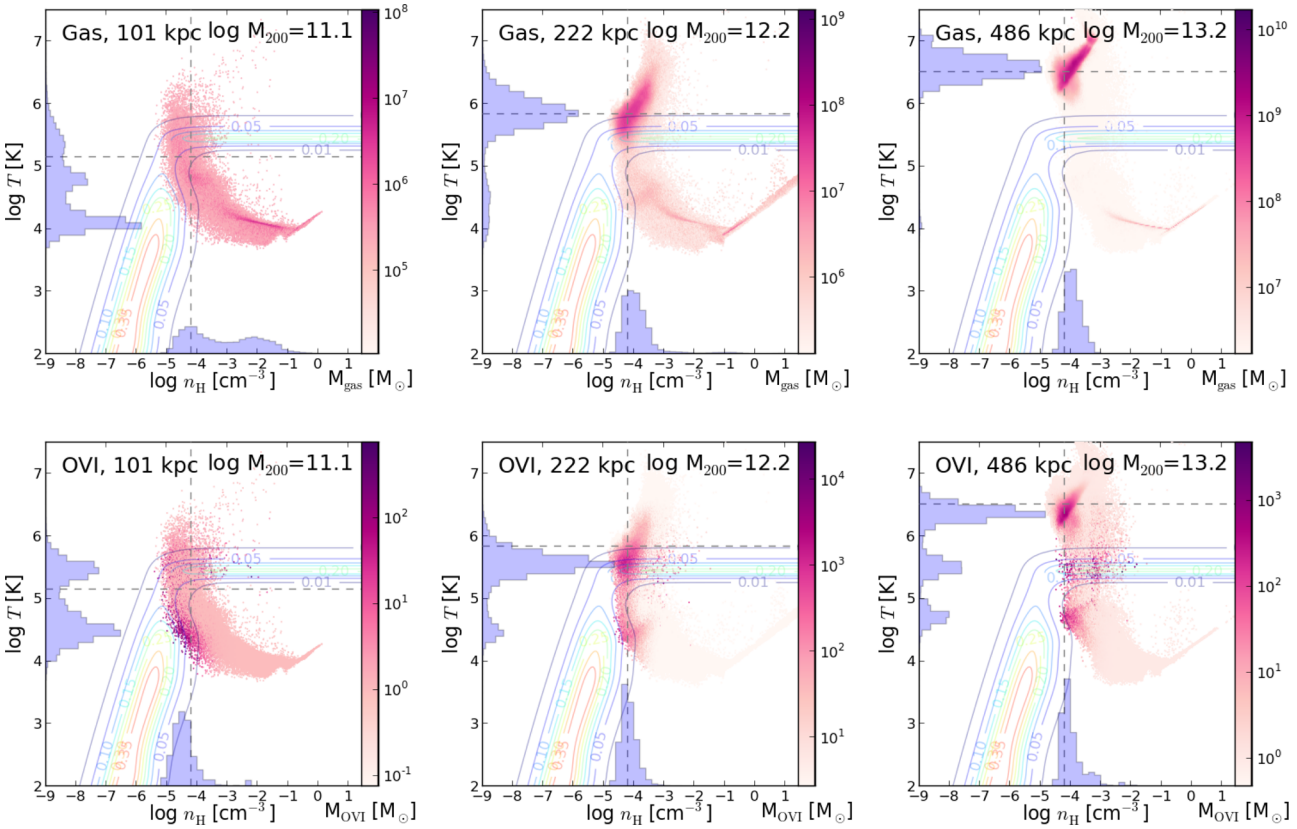

Figure 3. The mass distribution in the density–temperature phase space of the haloes shown in Fig. 2 at $z = 0.205$. The top row shows all gas within R_{200} (listed in the top left in kpc) and the bottom row shows only O VI. Histograms in each panel represent the probability density functions of gas density (bottom) and temperature (left). The dashed grey horizontal line indicates $T_{\rm vir}$ (equation 1), and the dashed grey vertical line indicates 200 × the critical overdensity. Contours show O VI ionization fraction levels with collisional ionization contours peaking at $10^{5.5}$ K, and photoionization contours at $<10^5$ K for lower densities.

The central galaxies have $M_* = 10^{9.0}$, $10^{10.4}$, and $10^{11.0}\,{\rm M}_\odot$, and typical SFRs for their masses.

We show hydrogen column densities in the top row with halo mass increasing from left-to-right. We plot the ρ–T diagnostic diagrams of all gas inside of R_{200} in Fig. 3 (top row), and see that the temperature histograms peak at $T_{\rm peak} = 10^{4.1}$, $10^{5.8}$, and $10^{6.6}$ K. We argue in Section 5 that the typical temperature of halo gas roughly follows that given by an isothermal, single-phase virialized halo,

$$T_{\rm vir} = 10^{5.69}\,{\rm K}\left(\frac{M_{200}}{10^{12}\,{\rm M}_\odot}\right)^{2/3}\left(\Omega_{\rm M}(1+z)^3+\Omega_\Lambda\right)^{2/3}, \qquad (1)$$

using the virial theorem. Using equation (1), we recover $T_{\rm vir} = 10^{5.1}$, $10^{5.8}$, and $10^{6.5}$ K (indicated by dashed grey horizontal lines in Fig. 3). For the sub-L^* halo, the $T_{\rm peak} \ll T_{\rm vir}$ owes to efficient cooling through the peak of the cooling curve to thermal equilibrium at $\sim 10^4$ K, although there does exist a tertiary peak near $T_{\rm vir}$. The more massive haloes have peak temperatures more similar to $T_{\rm vir}$.

The virial radius across these haloes increases by nearly a factor of 5 from 101 to 486 kpc, meaning that the adoption of a constant radius for the CGM, often assumed to be 300 kpc (e.g. Rudie et al. 2012; Ford et al. 2013), samples only the inner region of a group halo, but includes the diffuse IGM for a sub-L^* halo. It is important to remember that the ratio of the impact parameter to the virial radius varies significantly across a survey such as COS-Halos (Shull 2014).

The second row of Fig. 2 shows that oxygen columns increase with halo mass, and our overall sample indicates that there is an increase of $N_{\rm O}$ with M_* at all impact parameters, except at $b <$ 30 kpc where L^* galaxies have higher oxygen columns than groups. The mass of gaseous oxygen within a 300 kpc sphere increases by a factor of 40 as M_{200} increases by a factor of 100, with the greatest increase occurring from sub-L^* to L^* (17×), while L^* galaxies have the highest metallicities within 300 kpc ($Z/{\rm Z}_\odot = 0.11$, 0.36, 0.22; excluding star-forming gas does little to change these values).

The third row of Fig. 2 shows the column densities of O VI. It is striking that the L^* galaxies have by far the greatest O VI column density even though they do not have the highest gas and oxygen masses. The mass of O VI within a 300 kpc sphere increases by a factor of 9 from sub-L^* to L^*, but declines by a factor of 90 from the L^* to the group halo.

The bottom row divides the O VI map by the oxygen map to show the 'ionization fraction', which severely declines for the group halo. The global O VI fraction within a 300 kpc sphere falls from $x_{\rm O\,VI} = 2.8$ to 1.4 per cent from sub-L^* to L^*, and to 0.01 per cent for the group halo. O VI is merely the tip of the iceberg of the oxygen content in the CGM of star-forming galaxies. Meanwhile, the oxygen in group-sized haloes essentially disappears in the 'O VI filter'. The higher O VI fractions on the top left of the group halo (bottom right-hand panel) owes to a lower mass, foreground halo with higher CGM O VI.

The ρ–T diagrams of gas inside R_{200} in Fig. 3 clearly highlight the cause of this effect: groups exhibit virtually no gas below 2×10^6 K (upper right-hand panel). Regions with gas overlapped by O VI ionization fraction contours indicate where O VI can exist in significant quantities, and the O VI-traced gas is shown in the bottom panels. The triple-peak temperature histogram of the

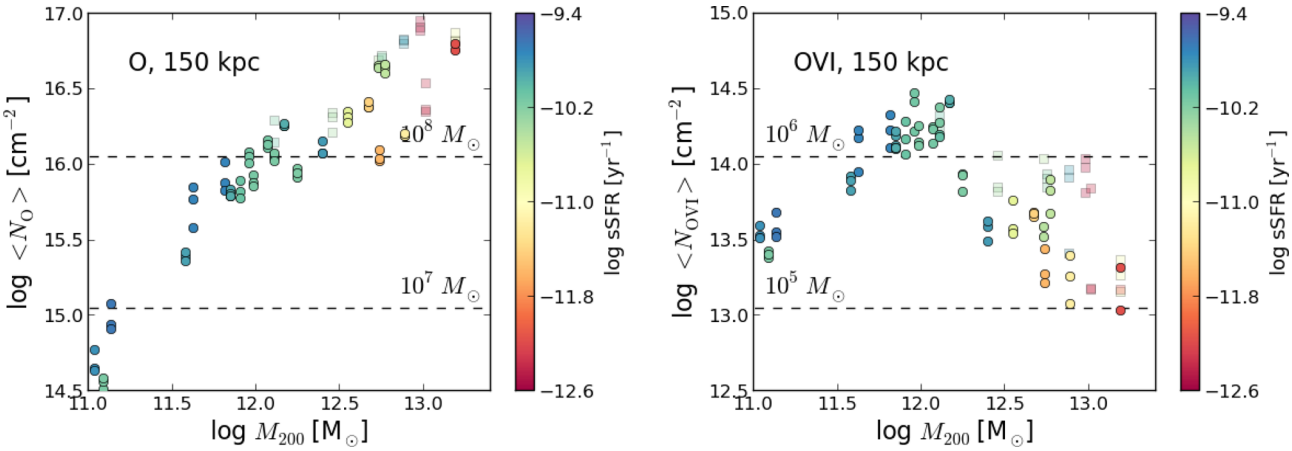

Figure 4. Aperture column densities within $b = 150$ kpc for oxygen (left) and O VI (right) as a function of halo mass at $z = 0.205$. Equivalent summed masses within 150 kpc are marked by dashed lines. Data points are coloured by sSFR, according to the colour bar on the right. Up to three data points for each halo are for three projections, with solid circles showing isolated projections and transparent squares that are lightly shaded indicating projections that do not satisfy the isolation criteria.

O VI distribution in the group (y-axis histogram, bottom right-hand panel) is common among our group haloes: metals at $T > 10^6$ K and $T < 10^5$ K are abundant due to longer cooling times but have $x_{\rm O\,VI} < 1$ per cent, while a small number of particles are rapidly cooling through the coronal regime (10^5–10^6 K) and briefly achieve $x_{\rm O\,VI} \sim 20$ per cent. In contrast, L^* halo virial temperatures, $T_{\rm vir} \sim 0.5$–1×10^6 K, overlap with the collisionally ionized O VI band at 3×10^5 K (bottom centre panel).

The sub-L^* CGM with gas between 10^4 and $\gtrsim 10^5$ K overlaps the photoionized O VI contours, which appear in gas $\lesssim 10^5$ K at lower densities (e.g. Shull, Smith & Danforth 2012). O VI peaks at a lower density ($n_{\rm H} = 10^{-4.5}$ cm^{-3}) in the photoionized regions of the sub-L^* halo than in the collisionally ionized regions of the L^* halo ($10^{-4.2}$ cm^{-3}). Oppenheimer & Davé (2009) showed that most O VI absorbers are photoionized using other SPH simulations, because the Haardt & Madau (2001) background is strong enough to photoionize IGM oxygen, which dominates the O VI absorbers found along intervening sight lines. The higher densities combined with hotter gas means that collisionally ionized O VI traces L^* CGM gas.

L^* haloes also have higher $N_{\rm O\,VI}$ (Fig. 2). To demonstrate that this is a broad trend across all of our haloes, we plot 150 kpc 'aperture' columns for oxygen (left) and O VI (right) in Fig. 4 for all galaxies, where we calculate the aperture column within a cylinder of radius $b = 150$ kpc by summing up pixel column densities, $N(x, y)$, as plotted in Fig. 2 according to

$$\langle N \rangle_b = \frac{\sum_{<b} N(x,y) {\rm d}x^2}{\pi b^2}\ {\rm cm}^{-2}, \quad (2)$$

where dx is the pixel size such that d$x \ll b$. We take aperture columns for each halo in three projections (along the x-, y-, and z-axis), and show isolated haloes as solid circles and non-isolated counterparts as transparent squares. $\langle N_{\rm O} \rangle_{150}$ increases monotonically across our halo mass range, while $\langle N_{\rm O\,VI} \rangle_{150}$ peaks for L^* galaxies and then declines sharply for $M_{200} > 10^{12.3}$ M$_\odot$. The average $\langle N_{\rm O\,VI} \rangle_{150}$ for the L^* range ($M_{200} = 10^{11.7}$–$10^{12.3}$ M$_\odot$) is $10^{14.23}$ cm^{-2} corresponding to an integrated O VI mass of 1.5×10^6 M$_\odot$ within a cylinder of radius 150 kpc. The corresponding values for groups ($M_{200} = 10^{12.3}$–$10^{13.3}$ M$_\odot$) are $10^{13.50}$ cm^{-2} and 2.8×10^5 M$_\odot$, or five times lower. We use only isolated galaxies in these calculations, but by including non-isolated projections, the $\langle N_{\rm O\,VI} \rangle_{150}$ in group-sized haloes rises to $10^{13.69}$ cm^{-2}, while that of L^* haloes does not change. $\langle N_{\rm O} \rangle_{150}$ equals $10^{15.99}$ cm^{-2} for L^* haloes and $10^{16.51}$ cm^{-2} for group haloes using isolated samples.

3.2 Circumgalactic radial profiles

To better understand the halo trends of the CGM distributions with mass, we show in Fig. 5 physical gas properties as a function of fractional virial radius at $z = 0.205$. The top left-hand panel shows $n_{\rm H}$ including all gas (CGM+ISM) as a function of r/R_{200}. We use thick lines to indicate the mean profiles for sub-L^* ($M_{200} < 10^{11.7}$ M$_\odot$, blue), L^* ($10^{11.7} \leq M_{200} < 10^{12.3}$ M$_\odot$, aquamarine), and group-sized ($M_{200} \geq 10^{12.3}$, orange) haloes. Sub-L^* galaxies achieve the highest inner densities and the lowest outer densities, while for groups the inner radial profiles ($\lesssim 1/3 R_{200}$) are nearly flat. ISM gas, defined as gas having SFR > 0, is not included in these plots, so there is more dense CGM gas around the lower mass galaxies that have higher sSFR. However, the density of extended 'coronal' gas ($1/3 R_{200} \lesssim r \lesssim R_{200}$) is higher for group haloes, owing to inefficient cooling at $>10^6$ K enabling them to retain higher pressure gas. All haloes are centred on the minimum of the gravitational potential, although one $10^{12.9}$ M$_\odot$ halo is undergoing a major merger, causing the density to dive inside $1/3 R_{200}$ and neither galaxy coincides precisely with the potential minimum.

The gas metallicities in the top right-hand panel are highest for L^* haloes in the centre, lower for sub-L^* throughout the entire halo, and lower for group haloes in the inner regions. The curves for individual haloes are noisier in this plot compared to the density plot, because satellite galaxies influence radial metallicities more than radial densities; groups have the greatest number of satellites and thus more peaks overall. The bottom left-hand panel showing the radial O VI fraction ($x_{\rm O\,VI}$) shows as strong of a trend of any of the panels in Fig. 5. The peak in $x_{\rm O\,VI}$ moves to larger fractional radius and declines with increasing halo mass. The sub-L^* galaxies achieve $x_{\rm O\,VI}$ as high as 10 per cent at $\sim R_{200}$, because the lower pressures allow oxygen at photoionized O VI temperatures, and therefore greater O VI fractions (Oppenheimer & Davé 2009). The L^* haloes have little scatter in $x_{\rm O\,VI}$, only reach $x_{\rm O\,VI} \sim 3$ per cent at R_{200}, and peak just beyond R_{200}. This is almost all collisionally ionized O VI, and the maximal radial $x_{\rm O\,VI}$ is $\sim$5 per cent, with only a fraction of oxygen residing around $10^{5.5}$ K. At $M_{200} > 10^{12.3}$ M$_\odot$, $x_{\rm O\,VI}$

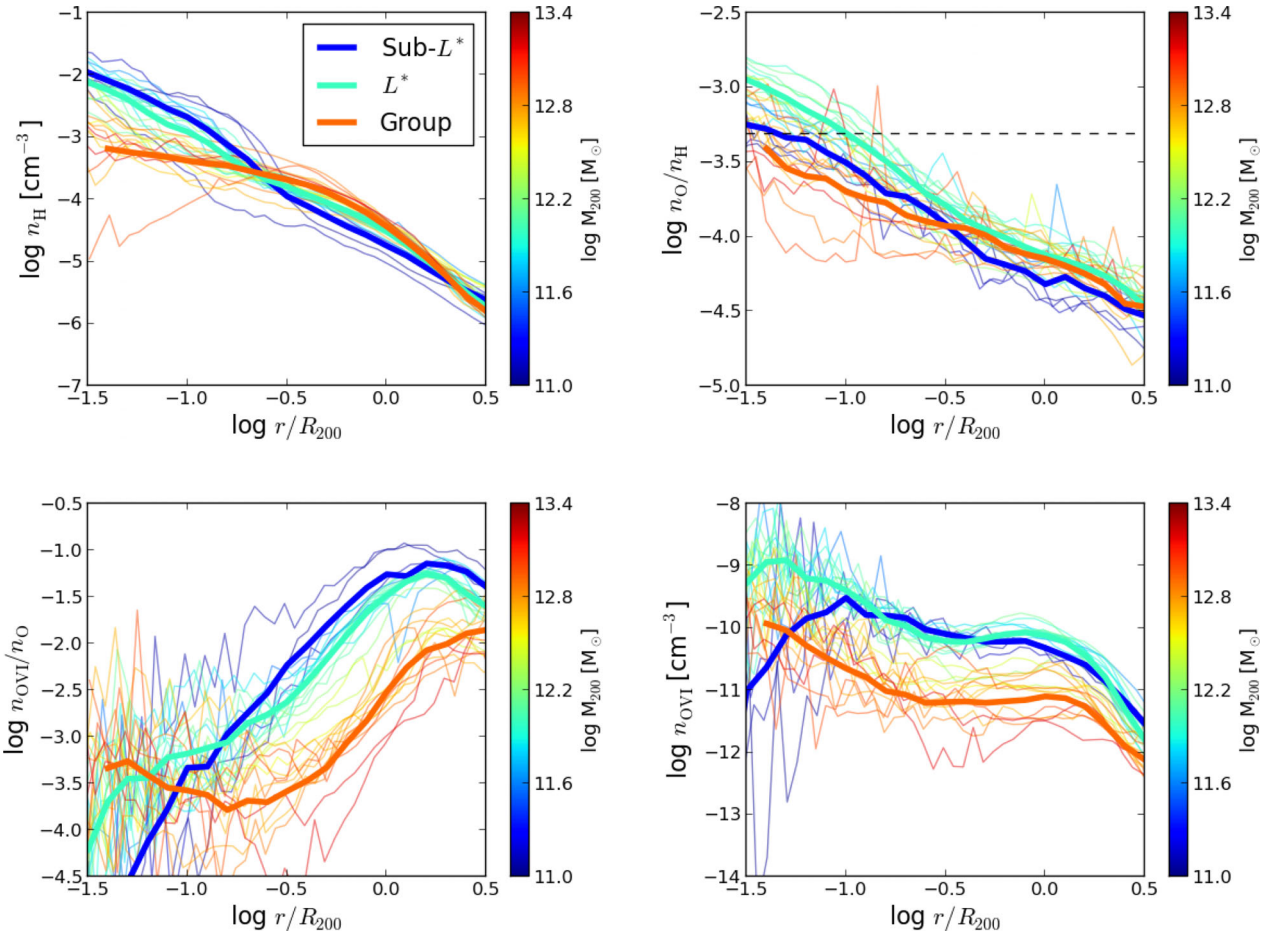

Figure 5. Radial profiles averaged in spherical shells of the hydrogen density (n_H), oxygen abundance (n_O/n_H), O VI ion fraction ($x_{O\,VI} \equiv n_{O\,VI}/n_O$), and O VI density ($n_{O\,VI}$) as a function of fractional virial radius from top left to bottom right at $z = 0.205$. Individual haloes are shown as thin lines, and thick solid lines represent averages of sub-L^*, L^*, and group-sized haloes (blue, aquamarine, and orange). The dashed line in the top right-hand panel indicates the solar oxygen abundance ($n_O/n_H = 10^{-3.31}$). Lower mass haloes have higher densities in their centres (top left), and L^* mass haloes have the highest oxygen abundances in their centres (top right). $x_{O\,VI}$ (bottom left) shows a strong trend with halo mass. Sub-L^* haloes ($<10^{11.5}$ M$_\odot$) have the highest $x_{O\,VI}$ owing to higher photoionized fractions, but this photoionized phase is greatly reduced in L^* haloes owing to higher pressures. Instead, L^* haloes are dominated by collisionally ionized O VI, and ion fractions only reach ∼5 per cent at radii just beyond R_{200}. Group haloes have even lower $x_{O\,VI}$ because the vast majority of the gas is too hot for O VI, and only gas beyond R_{200} approaches $x_{O\,VI}$ of several per cent. The bottom right-hand panel, showing O VI densities, is the product of the previous three panels, and shows the higher O VI densities for sub-L^* and L^* haloes than for group haloes.

essentially nosedives, owing to hotter temperatures. Collisionally ionized O VI does exist at $\sim 10^{5.5}$ K in group haloes, but the higher pressures mean higher densities, leading to faster cooling times through this temperature regime.

The product of the first three panels, $n_{O\,VI}$, is plotted in the bottom right-hand panel of Fig. 5. The highest O VI densities are associated with L^* galaxies, with $n_{O\,VI}$ peaking just inside R_{200}. The O VI mass as a function of radius peaks outside R_{200}, since although the density is lower, the volume increases as $4\pi r^2$.

3.3 Nature and origin of circumgalactic oxygen

Thus far we have focused on the trends of oxygen and O VI with halo mass, and we now shift our focus to the distribution and origin of oxygen-enriched gas in the CGM. We plot the oxygen content as a function of radius for our standard L^* haloes in the top left-hand panel of Fig. 6. Green shading on the bottom shows the O VI fraction of the oxygen budget peaking between one and two R_{200}, which are represented by vertical dotted lines. It is notable that there are five oxygen ions with greater contributions than O VI, and that O VI is one of the most spatially extended ions. This is the general result for L^* haloes, O VI resides primarily beyond R_{200} or at ∼200–500 kpc. This suggests that a significant fraction of the O VI detected by COS-Halos at $b < 150$ kpc likely arises at physical radii larger than R_{200}.

In the bottom left-hand panel of Fig. 6, we show the 'age' of the CGM, by plotting the last time a CGM particle was in the ISM of a galaxy, which is defined as the last time the gas particle was star forming (either in the central galaxy or a satellite). The vast majority of metals in the CGM were previously in the ISM and launched by superwind feedback into the CGM as found in other SPH simulations (Crain et al. 2013; Ford et al. 2014). The grey shading shows the oxygen-weighted age distribution as a function of radii, showing an age–radius anticorrelation, where larger radii and lower overdensities are enriched by higher redshift progenitors when halo potentials are lower and comoving distances are physically smaller (Davé & Oppenheimer 2007; Wiersma et al. 2010; Oppenheimer et al. 2012; Crain et al. 2013; Ford et al. 2014). O VI has a mean enrichment redshift of $z \sim 1.2$ at 300 kpc. Our simulations suggest that the average age of O VI is ∼6 Gyr, and it is thus not

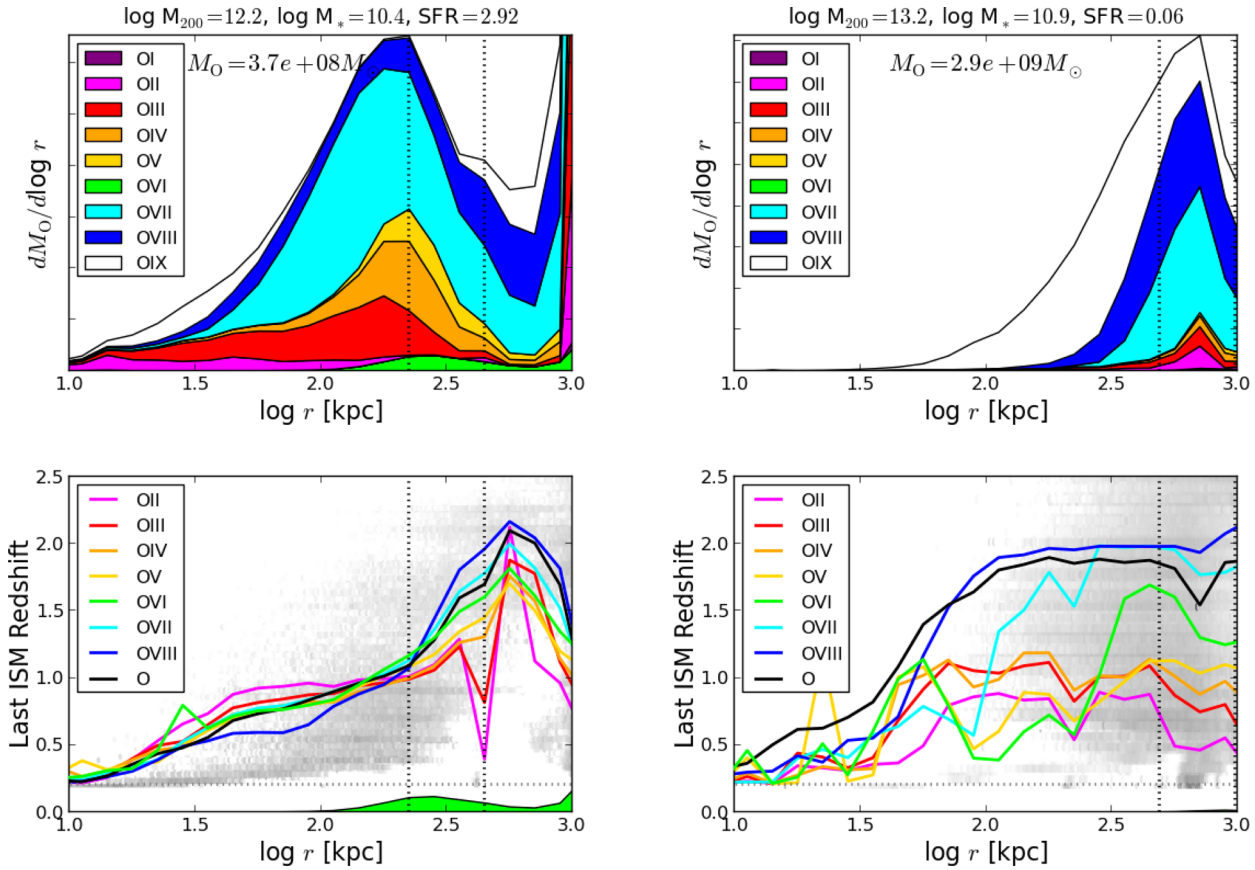

Figure 6. CGM oxygen as a function of radius is plotted in the top panels for the Gal005 L^* halo (left, $M_{200} = 10^{12.2}$ M$_\odot$) and the Grp008 group-sized halo (right, $M_{200} = 10^{13.2}$ M$_\odot$). The top solid line indicates the total oxygen content as a function of radius on a linear scale (*y*-axis values not specified). The total CGM oxygen content in each panel between $10^{1.05}$ and $10^{2.95}$ kpc is 3.7×10^8 and 2.9×10^9 M$_\odot$ for the L^* and group haloes, respectively (listed on the top of each panel). The dotted vertical lines indicate R_{200} and $2R_{200}$. The bottom panels indicate the age distribution of oxygen in grey shading, where we define age as the last redshift an SPH particle was in the ISM. The mean ages of oxygen species (coloured lines) and total oxygen (black line) are also shown. The grey horizontal dotted line is the redshift of the snapshot. We also repeat the O VI shading from the top panels in the age panels. O VI in L^* haloes primarily resides outside R_{200} and is greater than 5 Gyr old ($z > 1$). Group-sized haloes enrich a more extended region at earlier times ($z \sim 2$).

associated with the on-going SF traced by observational indicators, which probe galactic star formation on a much more recent timescale, i.e. $\lesssim$100 Myr.

In the right-hand panels of Fig. 6, we plot the relative oxygen content and age distribution around our largest group. The O VI is hardly visible on this linear plot, peaking at nearly $2R_{200}$. This group halo is dominated by ions that are only observable in the X-ray, with O IX dominating within R_{200}. By plotting the oxygen distributions on a physical rather than fractional virial scale, we emphasize the stark contrast between the linear distributions of oxygen between L^* and group haloes within 1 Mpc. The progenitors of this central passive galaxy have injected most of their metals at $z \sim 2$ where they now reside at larger radii relative to the L^* haloes, both in terms of physical distance and fractional virial distance.

4 COMPARISON TO COS-HALOS DATA

We confront the COS-Halos observational survey using our new PYTHON module called Simulation Mocker Of Hubble Absorption-Line Observational Surveys (SMOHALOS). We use SMOHALOS to create mock COS-Halos surveys using observed impact parameters for galaxies with similar properties as observed by COS-Halos, which in this case are defined by M_* and sSFR. This enables us to take the latest dataset from COS-Halos with updated spectroscopic galaxy observations (e.g. Werk et al. 2012), and make a mock survey with matched properties.

We do not constrain our mock galaxies to have the same redshifts as COS-Halos ($z = 0.15$–0.35). Instead, we select the *M5.3* simulated galaxy with the most similar M_* and sSFR that are closest to the observed values from as many as six output redshifts ($z = 0.250, 0.205, 0.149, 0.099, 0.053, 0.0$) for which we have run our NEQ zooms for a sufficient time ($t > 300$ Myr). Our galaxies evolve little over this redshift, except for the cases where there are mergers. We find that the O VI does not evolve significantly over this redshift range either, which we discuss later. The main rationale for this choice is to obtain more passive galaxies that satisfy the isolation criteria, because neighbours are either beyond 300 kpc at earlier snapshots, or, more often, merge into a single galaxy to satisfy the isolation criteria at later snapshots. Also, we did not output snapshots between $z = 0.25$ and 0.35. Fig. 1 shows galaxies that are isolated in one of three projections as solid circles. We have in total 123 L^* and group galaxies across six redshifts and 20 zoom simulations, 87 of which are isolated in all three projections, and 108 of which are isolated in at least one projection. One group halo is not isolated in any projection (Grp005).

We use the T11 list of COS-Halos galaxies, omitting the two least massive galaxies along each of the J0042−1037, J0820+2334, and J0943+0531 sight lines ($M_* < 10^{9.5}$ M$_\odot$), since we do not

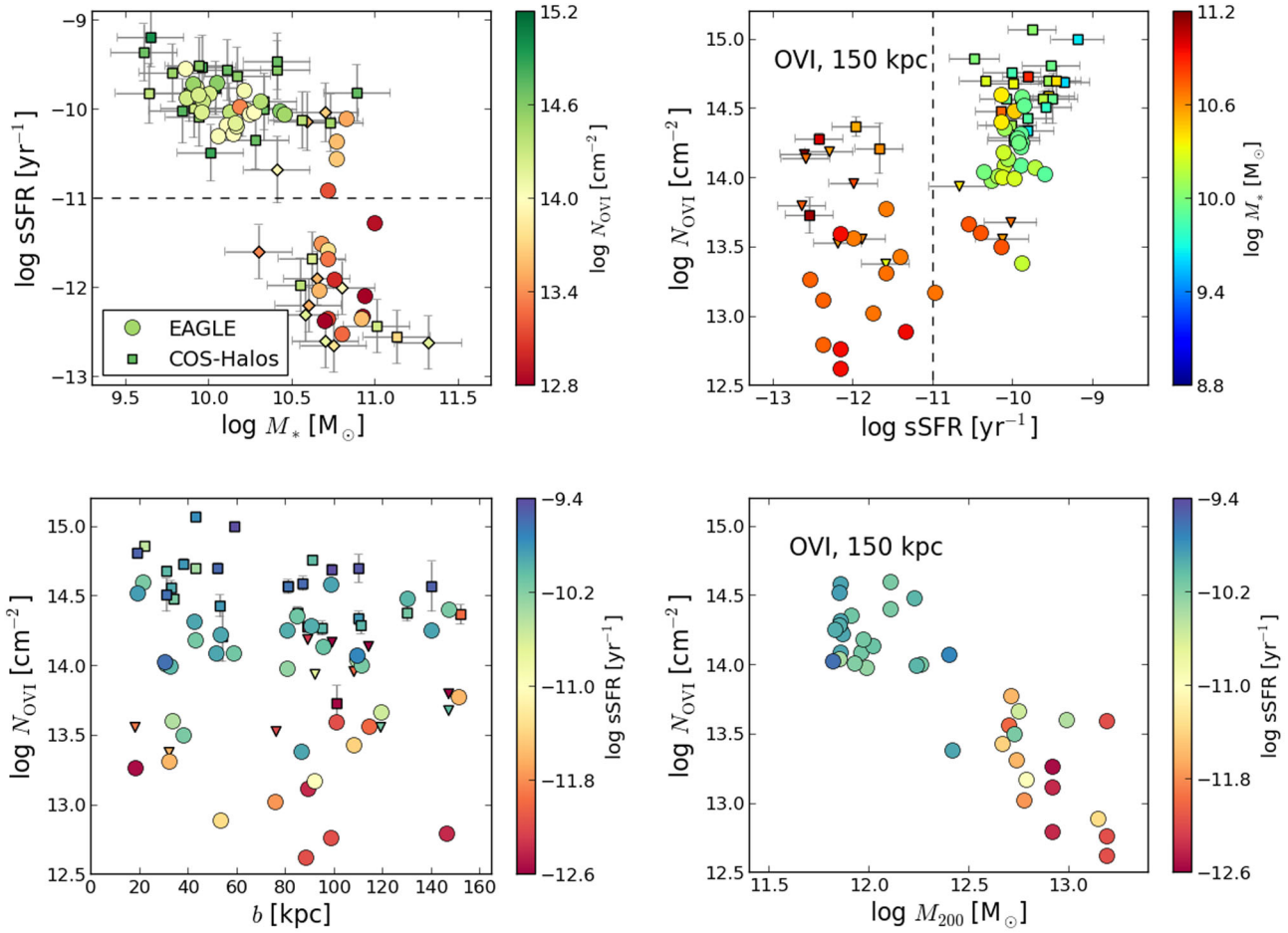

Figure 7. Comparisons of the COS-Halos dataset (squares are detections, triangles pointing down are upper limits) to a mock COS-Halos survey (circles). We choose the simulated galaxy that is closest to the given COS-Halos galaxy in terms of M_* and sSFR, and choose the same impact parameter, b, as the observed galaxy in a projection for which the galaxy would be defined as isolated from other L^* galaxies. The top left-hand panel shows real and mock observations on the M_*–sSFR plane, coloured by O VI column (diamonds here indicate galaxies with O VI upper limits). The top right-hand panel plots $N_{\rm O\,VI}$ as a function of sSFR, coloured by M_*. The bottom left-hand panel shows $N_{\rm O\,VI}$ as a function of b, coloured by sSFR. The bottom right-hand panel shows only the mock dataset coloured by sSFR to demonstrate how O VI columns change as a function of halo mass in a mock COS-Halos survey. Dashed lines in the top panels indicate the division between active and passive galaxies using an sSFR cut-off of 10^{-11} yr^{-1}.

explicitly simulate such masses, which leaves 39 galaxies in the COS-Halos sample. Stellar masses assume a Chabrier (2003) IMF, which decreases the stellar masses reported by Werk et al. (2012) by 0.2 dex, who assumed a Salpeter (1955) IMF.

We take 1σ errors on M_* and sSFR, where we assume $\delta M_* = 0.2$ dex and use the Balmer-derived SFR and error from Werk et al. (2012) to calculate the total error on the sSFR, which are added in quadrature to the error on M_* resulting in δsSFR = 0.30–0.37 dex. SMOHALOS applies a Gaussian dispersion seeded by a random number to the values of the simulated galaxies for the given impact parameter. We choose the simulated galaxy closest on the M_*–sSFR plane to the observed galaxy given the errors. We run 100 such realizations of SMOHALOS to construct 100 simulated COS-Halos galaxy samples using different random number seeds.

Fig. 7, top left, shows a typical SMOHALOS mock sample, plotted as circles, on the M_*–sSFR plane, with the COS-Halos galaxies plotted as squares for galaxies with O VI detections and diamonds for galaxies with O VI upper limits. Error bars indicate uncertainties on observations. The galaxies are colour coded by their O VI columns in both cases. It is immediately apparent that while our galaxies generally reproduce the star-forming and passive distributions seen by COS-Halos, we do not always obtain the same range of properties. For example, we do not create galaxies with $M_* > 10^{11.0}$ M$_\odot$, whereas three of these exist in COS-Halos.

The top right-hand panel shows O VI column density as a function of sSFR, coloured by M_*, and the bottom left-hand panel shows O VI columns as a function of impact parameter, coloured by sSFR (COS-Halos detections are squares and triangles pointing down are upper limits). The COS-Halos trend of O VI columns increasing with sSFR is reproduced. However, our mock O VI columns are too low compared to those inferred from COS-Halos, both as a function of sSFR and impact parameter.

We plot the SMOHALOS O VI columns against halo mass in the bottom right-hand panel of Fig. 7 to show that O VI correlates strongly with M_{200}, even more so than with the central galaxy sSFR (top right-hand panel). This plot nearly mirrors the trend of the 150 kpc aperture columns in Fig. 4, in part because there is not much dependence of $N_{\rm O\,VI}$ on impact parameter. However, there is greater scatter when choosing pencil beams corresponding to individual sight lines rather than taking an averaged aperture column. The colour coding of symbols in both plots indicates that the scatter in group sSFR primarily contributes to the reduced correlation in the $N_{\rm O\,VI}$–sSFR

relation relative to that in the $N_{\rm O\,VI}$–M_{200} relation. We suggest that the trend of $N_{\rm O\,VI}$ with sSFR found by COS-Halos is driven by halo mass rather than star formation activity.

We plot the probability distributions of the 100 SMOHALOS runs in the top two panels of Fig. 8 as grey shading and superimpose the results of the COS-Halos survey, again as coloured squares and upper limit triangles. The top panel shows that we consistently identify a bimodal set of galaxies in the M_*–sSFR plane. The middle panel shows that the SMOHALOS mock catalogues consistently reproduce the O VI–sSFR correlation, although the column densities are lower than for COS-Halos.

Subdividing galaxies into star forming and passive samples using an sSFR cut of 10^{-11} yr^{-1}, SMOHALOS recovers a median $\log[N_{\rm O\,VI}/{\rm cm}^{-2}] = 14.13$ for the 'blue' sample (27 galaxies) and 13.20 for the passive 'red' sample (12 galaxies). The corresponding COS-Halos numbers are 14.57 and $<$14.14, respectively, the latter being an upper limit, owing to most passive COS-Halos columns being non-detections. The typical column density of our blue sample is thus a factor of 2.8 $\times$ too low, and even if we take the SMOHALOS sample with the strongest median O VI column of the 100 realizations, $\log[N_{\rm O\,VI}/{\rm cm}^{-2}] = 14.27$, the column density is 2.0 $\times$ too low.

In the bottom panel of Fig. 8, we plot the average SMOHALOS radial O VI column density profiles of the star-forming (cyan) and passive (red) galaxies with shading indicating 1σ and 2σ dispersions using the 100 SMOHALOS realizations. We rarely reproduce columns in excess of $10^{14.5}$ cm^{-2} and never over $10^{15.0}$ cm^{-2} of which there are two detections in COS-Halos. Also apparent is the surprisingly flat dependence of O VI column on impact parameter for both star-forming and passive samples. When we subdivide the blue sample into two impact parameter bins, we find a larger difference in the interior CGM, such that median $\log[N_{\rm O\,VI}/{\rm cm}^{-2}]$ for COS-Halos and SMOHALOS are 14.70 and 14.14 at 0–75 kpc, and 14.38 and 14.12 at 75–150 kpc, respectively. Our median mass calculation of O VI within 150 kpc is 1.3 $\times$ 10^6 M$_\odot$, which is about 2 $\times$ lower than 2.4 $\times$ 10^6 M$_\odot$ calculated by T11. We discuss this shortfall of O VI around star-forming galaxies in EAGLE in Section 6.1.

The interpretation of the comparison to the passive sample of 12 galaxies is more ambiguous owing to the COS-Halos non-detections. The median O VI column density may be consistent between COS-Halos and the SMOHALOS catalogues; however, we never produce O VI columns around passive galaxies in the range of $10^{14.2–14.4}$ cm^{-2}, as high as the three strongest COS-Halos passive detections. We suspect that our SMOHALOS sample may be cleaner of neighbours than COS-Halos sample, because observations can miss surrounding galaxies owing to surface brightness limits. This was for example the case for the J2257+1340 sight line where two smaller star-forming galaxies were subsequently observed closer to a $10^{10.9}$ M$_\odot$ passive galaxy at 114 kpc (Tumlinson et al. 2013). Group galaxies with neighbours have higher aperture column densities, $\langle N_{\rm O\,VI}\rangle_{150} = 10^{13.76}$ cm^{-2}, than for isolated ones, $10^{13.50}$ cm^{-2}.

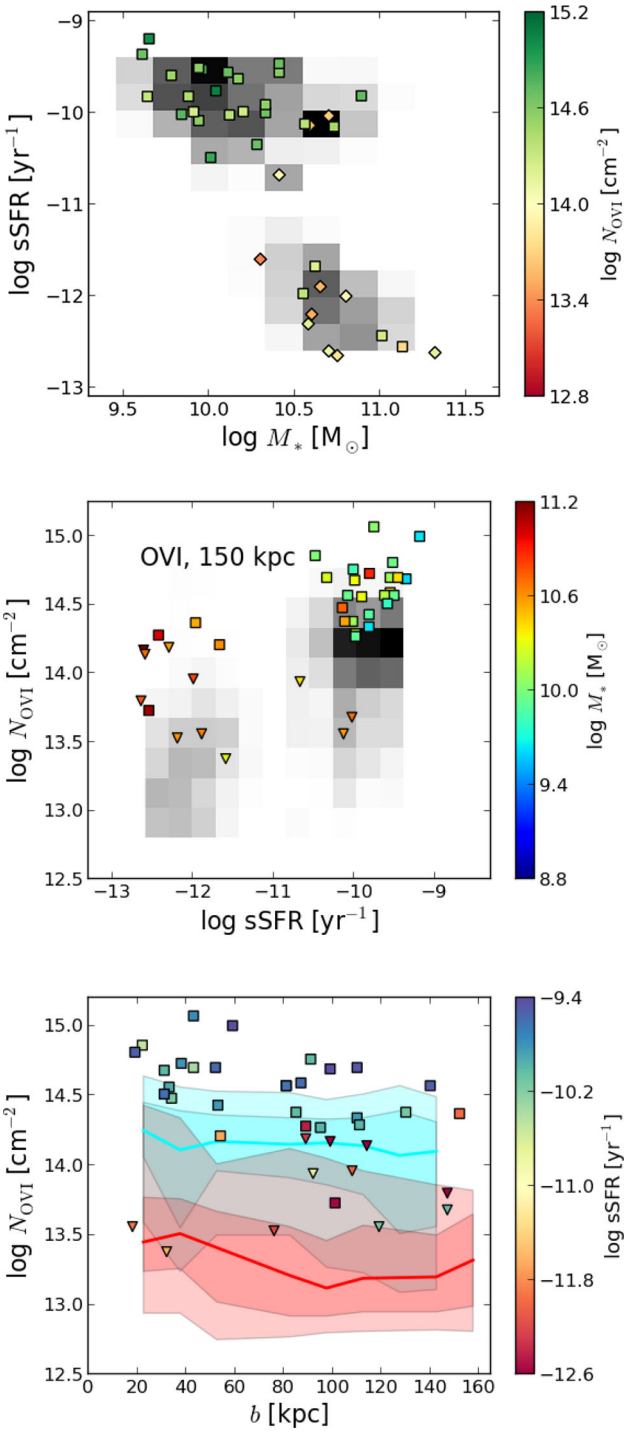

Figure 8. Probability distributions of mock observations from 100 SMOHALOS realization displayed in grey shading on a linear scale on the M_*–sSFR plane (top panel) and the $N_{\rm O\,VI}$–sSFR plane (centre panel). COS-Halos data are plotted as in Fig. 7, but without error bars. The bottom panel shows median $N_{\rm O\,IV}$ as a function of impact parameter for the star-forming (cyan) and passive (red) SMOHALOS samples, including darker and lighter shading for 1σ and 2σ dispersions. There is hardly any overlap of the 1σ dispersions between the star-forming and passive samples.

5 THE OXYGEN CONTENT OF GALACTIC HALOES

We now consider the total amount of oxygen formed in galaxies, and the phases this metal occupies at $z = 0.2$. Following Peeples et al. (2014, hereafter P14), we normalize the total mass of oxygen nucleosynthesized and ejected by stars to unity for each of our galaxies, and plot the fraction of oxygen found in stars (red), the ISM (blue), and the CGM (green) in Fig. 9. Where P14 plotted a continuous distribution as a function of stellar mass based on observed metal

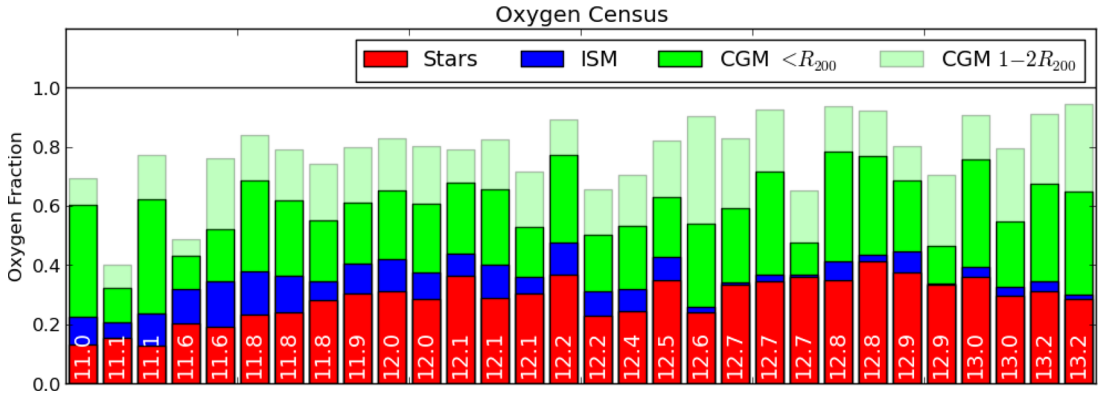

Figure 9. The oxygen budget for zoom haloes ordered by halo mass ($\log[M_{200}/\mathrm{M}_\odot]$ indicated by rotated white numbers), where the amount of oxygen produced and released by all galaxies within R_{200} is normalized to one. The relative oxygen content in stars (red), the ISM (blue), and the CGM (within R_{200}, bright green; at 1–$2R_{200}$, faded green) is then summed relative to the total oxygen production, as in P14. For L^* and group haloes, there exists more oxygen in the CGM within $2R_{200}$ than in the galaxy (stars+ISM) itself. Up to half the oxygen generated by an L^* galaxy can be ejected beyond R_{200}. One difference with P14 is that we sum the stellar and ISM oxygen content for all (central and satellite) galaxies in the halo, where P14 only include the central galaxy for these quantities.

abundances scaled to expected nucleosynthetic yields, we plot bars for our individual galactic haloes and order them by increasing M_{200}, listed in white at the bottom of each bar. Our mass distribution is not continuous, and the group-sized haloes are selected to have a large scatter in the baryon fractions within R_{200}.

We measure that EAGLE oxygen yields are on average 2.7 per cent of M_* at $z = 0.2$. Even though EAGLE employs metallicity-dependent yields, this makes negligible difference for the summed oxygen yield. This value is nearly the same as found by P14 who adopted an oxygen yield of 1.5 per cent for the zero-age main-sequence and calculated an average multiple of 1.8 to account for the fact that ≈55 per cent of the stellar mass survives to $z = 0$, based on Leitner (2012) star formation histories (i.e. 1.5 per cent × 1.8 = 2.7 per cent). It is not surprising that these two calculations agree, because we are using similar yields tabulated by Wiersma et al. (2009b) as P14, and because we are self-consistently following the star formation histories accounting for stellar evolution.[2]

One difference with respect to P14 is that we plot the total oxygen generated by all galaxies residing in the galactic halo, instead of just the central galaxy. This makes a marginal difference for L^* and sub-L^* galaxies, but the difference is quite noticeable for group-sized haloes since the stellar mass becomes less dominated by the group central; less than half the stellar mass resides in the central for haloes of $M_{200} \gtrsim 10^{13.0}\,\mathrm{M}_\odot$. The ISM oxygen content in the four largest haloes is contributed almost entirely by satellites.

The stellar oxygen content (red bars) follows the P14 trend with L^* and group haloes having similar oxygen fractions in stars (their fig. 12), but our sub-L^* galaxies ($M_* \sim 10^9\,\mathrm{M}_\odot$) have marginally higher stellar oxygen content, which is consistent with the EAGLE-RECAL simulation (S15) exhibiting slightly higher stellar metallicities content than inferred observationally by Gallazzi et al. (2005). The ISM oxygen content increases at lower mass, owing to higher gas fractions; the stellar mass–ISM metallicity relationship (i.e. the MZR) in the EAGLE-RECAL prescription reproduces the observed decline with mass (Tremonti et al. 2004; Zahid et al. 2014). Thus far, the agreement is good between our zooms and the observations, because the EAGLE-RECAL prescription broadly reproduces the observed metal content of galaxies.

We now report the oxygen contents of the CGM within R_{200} and additionally between 1 and $2R_{200}$, which are not nearly as well constrained by observations (P14). Our main results are twofold: (1) there exists more oxygen in the CGM within $2R_{200}$ than in the stellar and ISM content of the galaxy, and (2) a significant fraction, sometimes more than half of the oxygen, is ejected beyond R_{200} for L^* galaxies.

The first result that more oxygen exists outside galaxies was also inferred by P14. Here, we are omniscient about the location of our simulated metals, and find that there is almost always more circumgalactic oxygen within $2R_{200}$ than in the galaxy (stars+ISM). We plot this CGM oxygen within $2R_{200}$ in Fig. 10 categorized by ion. The eight ions plotted (O I through O VIII) plus O IX (not plotted due to its unobservable nature) sum to unity. Ions lower than O VI dominate the CGM associated with sub-L^* and many L^* galaxies, while ions above O VI always dominate the CGM of group haloes, often at the 80–95 per cent level indicating the need for a wide-area space-borne telescope sensitive to soft X-rays to account for the diffuse oxygen around groups.

Even for L^* haloes, for which O VI is the strongest, O VI contributes only a small fraction of the oxygen content of the CGM, which reflects this ion's maximal ≈5 per cent radial ion fraction (Section 3.1). We plot the CGM within $2R_{200}$, because O VI barely shows up on a plot with the limit of $<R_{200}$. The most common ion is O VII, which makes up 23–50 per cent of the circumgalactic oxygen at $<2R_{200}$ between $M_{200} = 10^{11.8}$ and $10^{13.0}\,\mathrm{M}_\odot$. It is almost as if nature conspires to hide diffuse oxygen (and most oxygen generated by stars) from our telescopes, since O VI is the most 'easily' observable CGM ion. Nonetheless, O VI represents a powerful probe that we argue arises so strongly around L^* galaxies owing to its temperature tracing the virial temperature of L^* haloes.

In the bottom panel of Fig. 10 we plot the oxygen fractions assuming collisional ionization equilibrium at the virial temperature $T_{\rm vir}$ according to equation (1). Our simulated haloes are of course not isothermal out to $2R_{200}$, and show a far greater diversity of oxygen ionization states, which in part owes to the neglect of photoionization in this simplistic assumption, but most importantly owes to the complex temperature and density structure of the CGM. Nonetheless, our simulated O VI fractions decline at a similar halo

[2] Oxygen that was first released and then trapped in the remnants of another generation is included.

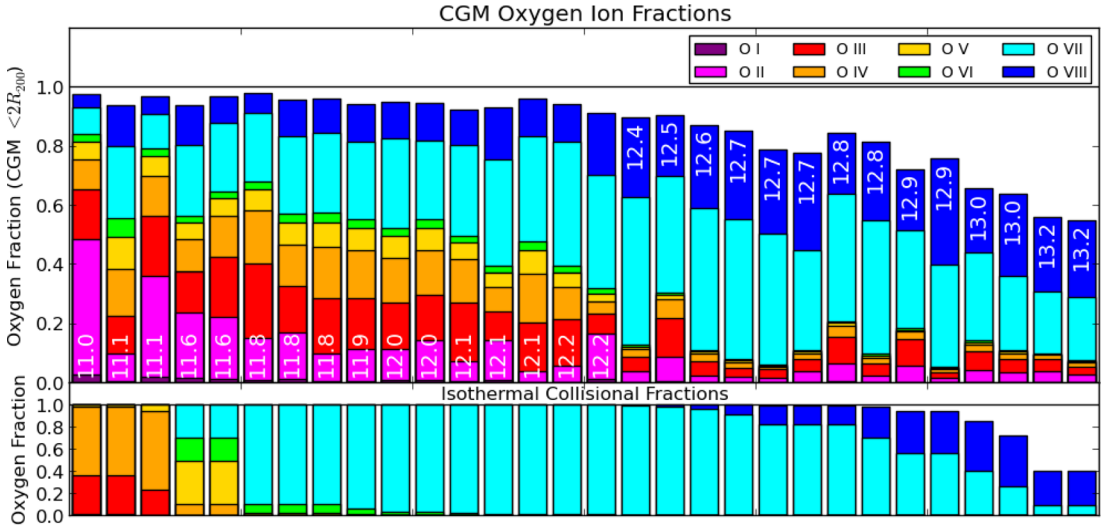

Figure 10. Top panel: bars indicate the ion fractions of the CGM oxygen within $2R_{200}$ in *M5.3* haloes ordered by M_{200}. This plot normalizes the amount of CGM oxygen represented by the sum of the bright and faded green bars in Fig. 9 to one, and subdivides it into oxygen species. Eight species (O I–O VIII) are coloured, and O IX is the difference with between the end of the blue bar and the horizontal line at a value of one. Bottom panel: bars indicate the ion fractions if one assumes an isothermal halo with $T = T_{\rm vir}$ and collisional ionization equilibrium. These assumptions do not hold for simulated haloes, but the simulated O VI fractions transition at a similar halo mass, $10^{12.3}$ M$_\odot$, as the isothermal fractions predict.

mass, $\sim 10^{12.3}$ M$_\odot$, as this simple model predicts, which clearly supports our conclusion that O VI traces the virial temperatures of L^* haloes, and not those of group-sized haloes. Going to sub-L^* haloes, $\lesssim 10^{11.7}$ M$_\odot$, the simulated haloes do not show a decline in O VI as predicted by the isothermal model, because photoionization begins to dominate at these masses.

Hence, our second main result from Fig. 9 is that up to half of the oxygen generated by an L^* galaxy resides outside of R_{200} in the low-z Universe. The implications for galaxy formation models are profound. Not only is the closed-box model of galaxy growth inaccurate due to continuous accretion on to galaxies, the idea that galaxies return products of star formation to extended CGM reservoirs from which they can later re-accrete (e.g. Bower et al. 2006; Oppenheimer et al. 2010; Guo et al. 2011; Henriques et al. 2015) may also be incorrect. The median oxygen content inside R_{200} for group-sized haloes ($M_{200} = 10^{12.7–13.3}$ M$_\odot$) is 69 per cent, which is somewhat higher than that of L^* haloes ($M_{200} = 10^{11.7–12.3}$ M$_\odot$) at 62 per cent. The increase of metals retained in higher mass haloes should be expected as larger haloes have deeper potential wells and physically larger virial radii. However, the reverse trend may apply because group-sized haloes have more star formation at early times when the Universe is physically smaller and halo potentials are shallower, which allow winds to travel to greater comoving distances. Additionally, group-sized haloes contain multiple large galaxies with large satellites more likely to lose their metals from a group halo, because they currently reside further from the halo centre and additionally may have fallen in at late times. Therefore, the moderate increase in metals retained inside R_{200} from 10^{12} to 10^{13} M$_\odot$ haloes may represent several competing trends. Finally, the space between the top of the faded green bars and the black horizontal line in Fig. 9 is oxygen ejected beyond $2R_{\rm vir}$, which usually resides in the low-density IGM.

We further investigate the multiphase structure of the CGM by considering gas pressures at different temperatures. We plot pressure as a function of halo mass at 0.3 and 1.0 × R_{200} in Fig. 11. To calculate a pressure at a given radius and temperature, we take the median CGM gas density with a 0.1 dex spread in radius and temperature, and compute $P/k = n_{\rm H}T/(X_{\rm H}\mu)$, where k is the Boltzmann constant, $X_{\rm H}$ is the mass fraction of hydrogen, and μ is the mean molecular weight. For each of our haloes, we colour the circles by temperature and scale their areas in proportion to $\log(m/M_{200})$, where m is the mass within the temperature/radius bin.

The first point to note is that the CGM is multiphase, especially inside $0.3R_{200}$. In the L^* range, there are copious amounts of gas at $T < 10^5$ K (purple and blue circles) and $T \geq 10^6$ K (yellow, orange, and red circles). Very little mass exists at $10^{5.0}$ and $10^{5.5}$ K (cyan and green circles), because gas cools rapidly through this temperature regime. When the cooling times become longer at $T \lesssim 10^{4.5}$ K, gas is at a significantly lower pressure, which indicates this gas is not cooling isobarically. By the time the gas reaches 10^4 K where cooling times are long, it becomes closer to achieving pressure equilibrium with gas with 100× more thermal energy. Thus, the interiors of L^* haloes inhibit long-lived collisionally ionized, $T \sim 10^{5.5}$ K, O VI owing to rapid cooling through the coronal regime, as well as cool, $T < 10^5$ K, O VI owing to high pressures forcing cold gas to densities that are too high to be photoionized by the Haardt & Madau (2001) background. In contrast, at R_{200} where the densities are lower and the cooling times are longer, the dominant phase is $10^{5.5}$ K (green circles), where O VI is a more effective tracer of the gas.

Group haloes have pressures that are far too high to allow long-lived O VI at any radii $\lesssim 0.5R_{200}$, although a multiphase CGM exists where a small amount of cold $\sim 10^4$ K gas achieves similar pressures as much hotter $\sim 10^{6.5}$ K gas in some haloes. As for L^* haloes, the gas at R_{200} is less multiphase, and the dominant phase is near the O VI collisional peak temperature.

We overplot the pressures assuming the single-phase isothermal model profile where $\rho \propto r^{-2}$ and $T = T_{\rm vir}$ from equation (1) with dashed lines in Fig. 11. The pressures of the $T > 10^{5.5}$ K phase generally follow the approximate magnitude and the slope ($P \propto M_{200}^{2/3}$) of the model, although L^* haloes and below have lower pressures interior to $0.3R_{200}$, which was also shown by Crain et al. (2010). Even though the single-phase isothermal model is clearly an

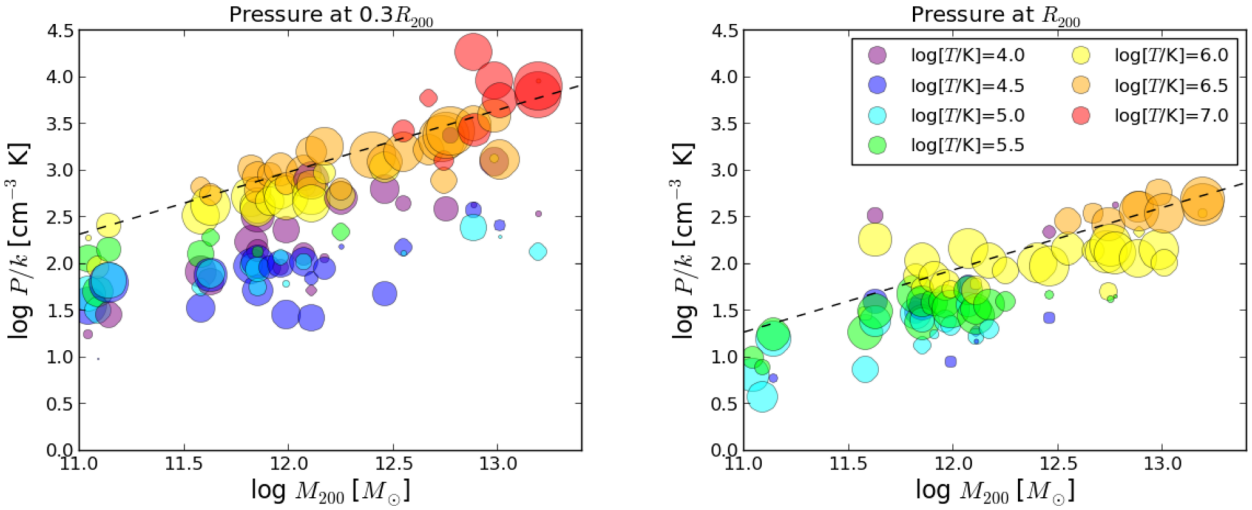

Figure 11. Pressure as a function of halo mass in shells at 0.3 × (left-hand panel) and 1.0 × R_{200} (right-hand panel). Pressures are calculated at a given radius and temperature by multiplying the median density within a 0.1 dex spread in r and T. The dashed lines indicate the pressure of an isothermal density profile at the virial temperature normalized to contain the entire baryonic content of a halo within R_{200}. The symbol areas scale in proportion to the logarithm of the mass, m, contained in this phase normalized to halo mass and radius, such that area $\propto \log[(m/M_{200})(r/R_{200})^{-2}]$.

incomplete description of the CGM, it provides useful insight into the trends for O VI. The high pressures of groups prevent a significant O VI-traced gas phase. While L^* haloes have the correct temperature for maximizing the fraction of collisionally ionized O VI, O VI still only traces a significant amount of mass in the exteriors where the coronal cooling times are long. Sub-L^* haloes have pressures low enough to allow photoionized O VI.

6 DISCUSSION

Our findings suggest that the O VI–sSFR correlation discovered by COS-Halos is an indirect correlation, and that the fundamental trend is O VI tracing virialized enriched gas at temperatures close to $10^{5.5}$ K, where the O VI fraction peaks. Passive central galaxies with mass $M_* \sim 10^{10.5}$ M$_\odot$ reside in higher mass haloes than active galaxies with a similar mass. The higher virial temperatures of the haloes hosting the passive galaxies lead to significantly lower O VI fractions. While the CGM metal content increases with halo mass, O VI is not an effective tracer of haloes with mass $\gg 10^{12}$ M$_\odot$. The CGM oxygen budget cannot be directly linked to recent star formation, which we demonstrated by showing that the typical age of O VI is greater than 5 Gyr and represents the cumulative ejection of metals by galactic superwinds over a Hubble time.

If the O VI were to trace metals originating from the star formation determined through observational indicators, then the time to travel to 150 kpc would imply a very high outflow speed. A >1500 km s^{-1} wind is necessary to travel this distance in <100 Myr, which is the timescale for the observed SF indicators to be linked to recent SF. Such high-velocity winds are rarely if at all present in our simulated L^* haloes at low-z, which is also supported by recent observations of outflows around star-forming galaxies in the evolved Universe. A number of campaigns have observed blueshifted, low-ion absorption wings extending to at most a few hundred km s^{-1} from the galaxy, almost always at velocities unable to escape the gravitational potential of the halo (e.g. Bouché et al. 2012; Martin et al. 2012; Rubin et al. 2014; Chisholm et al. 2015; Nielsen et al. 2015).

We predict the amount of metals residing in low-redshift CGM reservoirs to be larger than the amount of metals in galaxies including stars and the ISM. Despite the high O VI column densities around L^* galaxies, the summed O VI ionization fractions are only 0.9–1.3 per cent in CGM gas within R_{200} and increase to 2.2–3.4 per cent when including CGM oxygen within $2R_{200}$. This is still higher than the global IGM O VI correction of ∼1 per cent reported by Rahmati et al. (2016) for the EAGLE 100 Mpc box at low-z. Assuming $x_{\rm O\,VI} = 20$ per cent thus severely underestimates the CGM oxygen content. This is not surprising since collisionally ionized O VI has a very small temperature range around $10^{5.5}$ K where it approaches its maximal $x_{\rm O\,VI}$ of ≈20 per cent.

We emphasize the dramatic decline O VI takes as one transitions from L^* to group haloes, and note the strength of the $N_{\rm O\,VI}$–M_{200} correlation. The average O VI absorption within 150 kpc for *every* L^* halo in the range of $10^{11.7} < M_{200} < 10^{12.2}$ M$_\odot$ is higher than for *every* group halo in the range $10^{12.6} < M_{200} < 10^{13.3}$ M$_\odot$, where each subsample contains more than 10 haloes. The O VI column densities within 150 kpc decline by a factor of 5 when considering isolated galaxies, and by a factor of 3.5 when considering all galaxies, when transitioning from L^* to group haloes. In contrast, the oxygen columns within 150 kpc increase by nearly a factor of 3 for the isolated sample and by more than a factor of 4.5 for all galaxies moving to higher mass. Hence, the average O VI ionization fraction for the CGM inside R_{200} is almost a factor of 20 lower for group-sized haloes, such that $x_{\rm O\,VI} \sim 0.1$ per cent.

6.1 Shortfall of halo O VI around L^* galaxies

The inability of our simulated ions to reproduce the higher O VI column densities observed by COS-Halos around blue L^* galaxies is worth discussing in greater depth. As noted in Section 4, we find about 2 × too little O VI within 150 kpc using the *M5.3* zooms, with the greatest deviation being within 75 kpc (≈3 ×). We now discuss several possibilities of why there may be such a shortfall.

We note that our stellar masses are too low by a factor of ∼2 in these zooms compared with abundance matching constraints. In Appendix B, we explore the higher resolution *M4.4* zooms, finding that O VI is slightly stronger (0.06 dex) around L^* galaxies, but the stellar masses *decline* by 0.18 dex making a ≳3× discrepancy with abundance matching. Recalibrating the EAGLE model is necessary

at higher resolution, and it may be that through the generation of more stars, more oxygen is produced and ejected into the CGM, which creates even higher O VI column densities than in the *M4.4* zooms. Indeed, Rahmati et al. (2016) found that across different EAGLE models, the integrated metal ion column density distributions scaled nearly linearly with the integrated stellar mass. It may also be possible that there exists enough freedom in superwind feedback implementations to change O VI columns by a factor of 2, while still successfully reproducing the large array of galaxy observables at many redshifts as the EAGLE prescription does.

Another possibility is that the low stellar masses in our *M5.3* zooms could lead to a mismatched selection of overmassive haloes, where we have shown O VI to be weaker. To test this hypothesis, we run SMOHALOS where we artificially increase the *M5.3* stellar masses by 0.3 dex in accordance with abundance matching constraints, and find essentially no difference in the median O VI column densities. Hence, this cannot explain the O VI shortfall.

A third possibility is that the original COS-Halos galaxy-selected sample exhibits Malmquist bias, which we cannot replicate using SMOHALOS applied to a limited set of zoom haloes. The COS-Halos galaxies were selected photometrically, which can lead to a biased sample of higher star-forming and/or more massive galaxies from a Schechter function. While SMOHALOS attempts to match galaxies based on M_* and sSFR, we do not have a large enough sample to reproduce the high SFRs observed in COS-Halos (Werk et al. 2012). For example, 3 per cent of SMOHALOS galaxies have SFR $>3.0\,\mathrm{M_\odot\ yr^{-1}}$ compared to 18 per cent of COS-Halos, and we have no galaxies with SFR $> 5.0\,\mathrm{M_\odot\ yr^{-1}}$ compared to 8 per cent of the COS-Halos. Whereas COS-Halos selects star-forming galaxies from a large cosmic volume, our L^* zooms are selected from a 25-Mpc box. Hence, we may not produce the O VI absorption columns observed in COS-Halos, because we are not simulating the same galaxies.

Finally, we assume a slowly evolving extragalactic background (Haardt & Madau 2001) without any local sources of ionizing radiation. Ionizing radiation from nearby star formation can increase O VI columns as demonstrated by Vasiliev et al. (2015) who found that $x_{\mathrm{O\,VI}}$ can reach 0.4–0.9 and reproduce COS-Halos O VI observations, albeit under specifically chosen conditions conducive to the photoionization of O VI. This model could invalidate our conclusion that O VI traces the virial temperature of L^* haloes and not that of group haloes, because photo-ionization requires $<10^5$ K gas, although it could be argued that both cold gas and ionizing photons from star formation decline in group haloes. Suresh et al. (2015b) show that O VI can be significantly enhanced by local sources of ionizing radiation, but only within 50 kpc using a 100 per cent escape fraction for soft X-rays from a SFR $= 10\,\mathrm{M_\odot\ yr^{-1}}$ galaxy, which are unrealistic assumptions for COS-Halos.

However, we suggest the possibility that photoionization of O VI could be part of the solution, owing to fluctuating AGN 'flash' ionizing their CGM. Oppenheimer & Schaye (2013b) introduced the concept of AGN proximity zone fossils, where 'cool' 10^4 K gas is ionized by a halo's central AGN that subsequently turns off leaving the surrounding CGM overionized for a time similar to the recombination timescale of diffuse gas, which can equal or exceed the typical time between AGN episodes. They showed that Seyfert-level AGN that are on for 10 per cent of the time can enhance O VI levels by >1 dex after the AGN *turns off*. The effect may be particularly relevant for cool metals at $n_{\mathrm{H}} = 10^{-3}$–$10^{-4}\,\mathrm{cm^{-3}}$ where CGM metals exist in our simulations, and the relevant recombination timescales for O VI range from 2 to 20 Myr. Thus a short Seyfert 'burst' lasting ∼0.1–1 Myr within the past ∼10–20 Myr can enhance O VI at the expense of lower oxygen ions, which normally trace this gas in equilibrium with the Haardt & Madau (2001) field. The COS-Halos galaxies do not show AGN activity (Werk et al. 2012) and are thus in the off-phase. The O VI nearer to the AGN should be more enhanced by the proximity zone fossil effect, which would agree with COS-Halos data showing O VI increasing at small impact parameter more steeply than our SMOHALOS realizations. This hypothesis requires a significant fraction of COS-Halos blue galaxies to be recent AGN.

6.2 Effect of AGN feedback

To test the impact of AGN thermal feedback (i.e. not the proximity fossil effect discussed above) on CGM O VI, we run a single group halo (Grp004), which has $M_{200} = 10^{12.89}\,\mathrm{M_\odot}$ at $z = 0.205$, turning off SMBH growth and AGN feedback. This halo is the most frequently selected SMOHALOS passive galaxy. Fig. 12 compares 600 kpc snapshots of the standard run on the left versus the 'NoAGN' model on the right in the same sequence as Fig. 2. While stellar feedback still operates in the NoAGN run, the galaxy is 2.8 × more massive. There exists 2.8 × more hydrogen and 2.7 × more oxygen in the CGM inside R_{200} in the NoAGN model (cf. top two sets of panels). The values of $\langle N_{\mathrm{O}}\rangle_{150}$ are $10^{16.19}$ and $10^{16.65}\,\mathrm{cm^{-2}}$ with and without AGN, respectively, reflecting the nearly factor of 3 increase in CGM oxygen in NoAGN group haloes.

Considering the O VI column densities in the third set of panels, there exists 1.9 × more O VI within R_{200}, but there is substantially less (8 ×) O VI within a radial distance of 100 kpc in the NoAGN model. The values of $\langle N_{\mathrm{O\,VI}}\rangle_{150}$ happen to be very similar, $10^{13.26}$ and $10^{13.35}\,\mathrm{cm^{-2}}$ with and without AGN, respectively, which are both typical O VI columns for our simulated groups. Combined with the oxygen aperture columns, we show $x_{\mathrm{O\,VI}}$ is much lower in the NoAGN model (bottom panels), especially at small impact parameters. Our findings for this halo agree with the global IGM statistics of Rahmati et al. (2016) showing only small differences between the REF and NoAGN models, which we further discuss in Appendix B.

In contrast to Suresh et al. (2015b), who argue that the decline of O VI around passive versus star-forming galaxies of the same stellar mass owes primarily to AGN feedback removing mass from the haloes of passive galaxies, our exploration indicates that it is primarily an ionization effect that reduces O VI columns. Passive COS-Halos galaxies reside in higher mass haloes than their active counterparts, which have virial temperatures that are too high for O VI. Our NoAGN halo has almost 3 × as many stars in the central galaxy and CGM metals within R_{200} as the standard run, but, almost coincidentally, a similar amount of O VI owing to the lower $x_{\mathrm{O\,VI}}$ as a result of having less $10^{5–6}$ K gas in the inner halo. Another big difference is that the NoAGN run has a SFR $=6.8\,\mathrm{M_\odot\ yr^{-1}}$, which creates a type of isolated galaxy rarely observed in the $z \lesssim 0.2$ Universe.

7 SUMMARY

We have run a set of EAGLE zoom simulations to confront the O VI observations within 150 kpc of $z = 0.15$–0.35 star-forming and passive galaxies from the T11 COS-Halos observational campaign. Our main simulations use the same model and resolution as the EAGLE RECAL-L025N0752 run, but include the NEQ ionization and cooling module introduced by OS13 and Richings et al. (2014), which we activate at low redshifts. 20 zoom simulations, focusing on L^* haloes ($M_{200} = 10^{11.7}$–$10^{12.3}\,\mathrm{M_\odot}$) hosting star-forming galaxies,

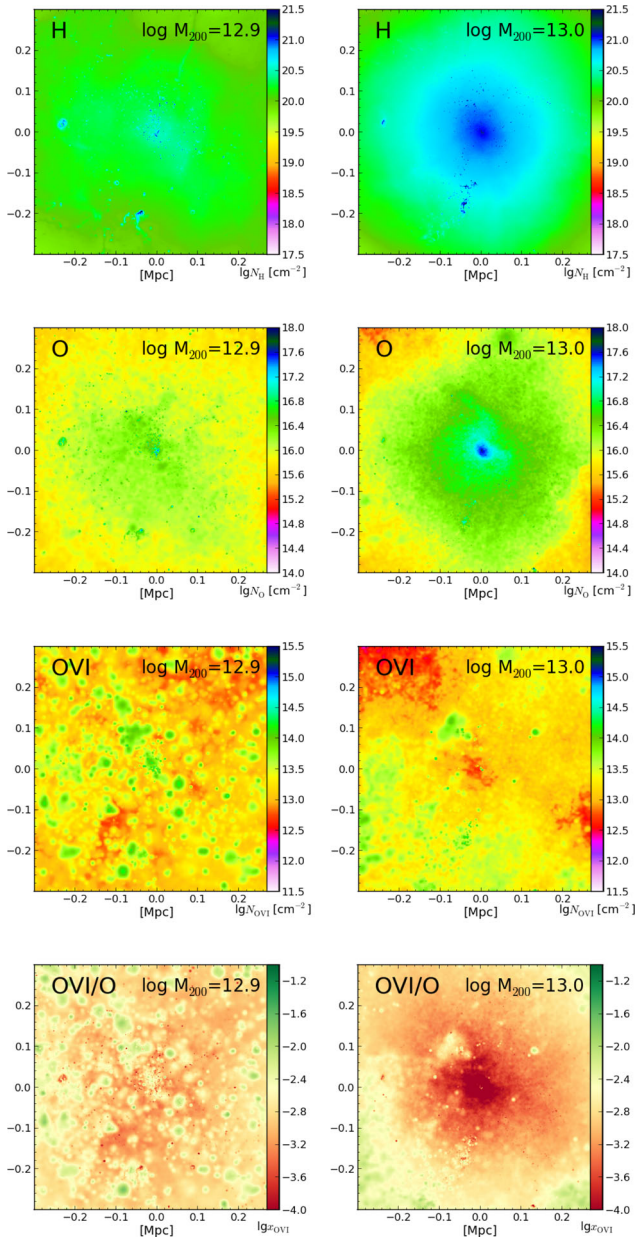

Figure 12. The same group-sized halo (Grp004, $M_{200} = 10^{12.89}$ M$_\odot$) at $z = 0.2$ simulated using the standard EAGLE prescription (left) and without AGN feedback model (right) in the same format as Fig. 2. From top to bottom, 600 kpc snapshots of hydrogen, oxygen, and O VI columns are shown as well as the O VI ionization fraction. The NoAGN halo has $M_{200} = 10^{12.97}$ M$_\odot$, compared to $10^{12.89}$ M$_\odot$ with AGN feedback due to weaker feedback, but we use a constant $R_{200} = 387$ kpc when comparing virial quantities.

and group-sized haloes ($M_{200} = 10^{12.7}$–$10^{13.3}$ M$_\odot$) mostly hosting passive galaxies, are simulated to $z = 0$ with the NEQ module activated at $z = 0.50$ and 0.28 for the L^* and group haloes, respectively. Our main results are as follows.

(i) Our simulations reproduce the observed correlation of circumgalactic O VI column density and sSFR (Figs 7 and 8).

(ii) The bimodality of the O VI column density, with higher column densities around star-forming galaxies than around passive galaxies, owes to the temperature of the virialized halo gas. The virial temperature of L^* haloes overlaps with the temperature at which collisionally ionized O VI peaks ($T \sim 10^{5.5}$ K), while virial temperatures of group-sized haloes are too high to be traced by O VI (e.g. Figs 4 and 6).

(iii) There is no direct link between star formation in the central galaxy and the O VI out to 150 kpc. The median age of the oxygen traced by O VI in the CGM is >5 Gyr, and represents the accumulation of circumgalactic metals over the entire star formation history of the galaxy.

(iv) The global O VI fractions of our L^* haloes range $x_{\rm O\,VI} = 0.9$–1.3 per cent, which means that far more oxygen exists in other ionization states, both lower and higher than O VI. Most O VI observed around L^* galaxies observed at impact parameters $b < 150$ kpc is at physical separations of $r = 200$–500 kpc ($\approx$1–$2R_{200}$) from the galaxy. The global L^* $x_{\rm O\,VI}$ rises to 2.2–3.4 per cent when considering oxygen out to $2R_{200}$, owing to optimal ionization O VI conditions at $\approx$1–$2R_{200}$ (Figs 6 and 10).

(v) Group haloes hosting passive galaxies often have global $x_{\rm O\,VI} \sim 0.01$ per cent inside R_{200}, and the majority of circumgalactic oxygen is completely ionized (O IX). Group haloes have average column densities of $N_{\rm O\,VI} = 10^{13.7}$ cm^{-2} for $b < 150$ kpc, which mostly arises from gas beyond R_{200}. This column density is 3.5 $\times$ lower than for L^* haloes ($10^{14.2}$ cm^{-2}). Applying isolation criteria similar to COS-Halos galaxies, the mean O VI column density around group centrals falls to $N_{\rm O\,VI} = 10^{13.5}$ cm^{-2}, which is 5 $\times$ lower than for isolated L^* haloes. Despite the low O VI column densities in groups, there exists 3 $\times$ more oxygen within a 150 kpc aperture than for L^* haloes.

(vi) Our simulated L^* haloes have O VI column densities that are $\sim$2 $\times$ too low compared to COS-Halos observations at $75 < b < 150$ kpc, and $\sim$ 3.5 $\times$ at $b < 75$ kpc. This could be related to an underproduction of total oxygen as our L^* stellar masses are 2 $\times$ too low relative to abundance matching constraints. Increased photoionization, possibly from proximity zone fossils due to fluctuating AGN (Oppenheimer & Schaye 2013b), are an unconsidered source that could increase the O VI ion fraction.

(vii) The majority of the oxygen produced and released by stars is ejected by superwind feedback beyond the optical extent of the galaxy, such that more oxygen exists in the CGM within $2R_{200}$ than in the galactic component (stars+ISM). The progenitors of L^* galaxies can eject more than half of their oxygen beyond R_{200} by $z = 0.2$, although the fraction of oxygen remaining within R_{200} (stars+ISM+CGM) averages 62 and 69 per cent for L^* and group haloes, respectively. Enrichment at large radii primarily occurs at high z, especially for group haloes, when gravitational potentials were shallower and fixed comoving distances were physically smaller (Figs 6 and 9).

(viii) O VII is the most abundant oxygen ion in the CGM for haloes between $M_{200} = 10^{11.8}$ and $10^{13.0}$ M$_\odot$, with between 23 and 50 per cent of the circumgalactic oxygen inside $2R_{200}$ ionized to O VII. This is a factor of 8–20 (60–190) higher than O VI in L^* (group) haloes (Fig. 10).

(ix) We explore the role of AGN by running a $10^{12.9}$ M$_\odot$ group halo without AGN feedback, finding that it produces similar O VI column densities at $b < 150$ kpc ($10^{13.3}$ cm^{-2}) as our standard group haloes with AGN feedback. Hence, the bimodality of circumgalactic O VI column densities with sSFR does not owe to the removal of mass and metals from the haloes of galaxies with more active black holes, but is clearly an ionization effect of reduced $x_{\rm O\,VI}$ in hot haloes (Fig. 12).

In our simulations, the higher O VI column densities around star-forming galaxies compared with passive galaxies are due to their

virial temperatures being more favourable for a high O VI fraction rather than to higher total oxygen column densities. A key test of this explanation would be to observe our prediction of the greater total oxygen content in the CGM of higher mass haloes, where O VI is no longer an effective tracer of CGM oxygen. Observing the soft X-ray ions O VII and O VIII out to the virial radius is beyond the scope of current facilities, although we will make predictions for upcoming facilities in future work. Unfortunately, absorption lines capable of tracing $>10^6$ K metals are at extreme UV energies, which shifts them out of the COS wavelength coverage at low redshift.

Our model contrasts with that of Suresh et al. (2015b), who predict that AGN blow more baryons out of haloes around passive than star-forming galaxies, and therefore will not predict more metals at $b \lesssim 150$ kpc around passive galaxies. Alternatively, photoionization by galactic sources (e.g. Oppenheimer & Schaye 2013b; Vasiliev et al. 2015) instead predicts that the O VI bearing material would exist in $\sim 10^4$ K gas around galaxies.

Our results indicate that O VI acts as a sensitive thermometer of halo gas, such that the O VI column density around star-forming and passive galaxies informs more about temperature than about the oxygen mass.

ACKNOWLEDGEMENTS

The authors would like to thank John Stocke, Mike Shull, Molly Peeples, Romeel Davé, Todd Tripp, Kristian Finlator, Brent Groves, and Andreas Pawlik for useful discussions contributing to this paper. We acknowledge Adrian Jenkins for providing the software for the generation of initial conditions. We also wish to thank the anonymous referee for improving the quality of the paper. Support for BDO was provided by NASA through grants HST-AR-12841 from the Space Telescope Science Institute, which is operated by the Association of Universities for Research in Astronomy, Incorporated, under NASA contract NAS5-26555, and the Astrophysics Theory Grant, 14-ATP14-0142. We acknowledge PRACE for awarding us access to resource Supermuc based in Germany at LRZ Garching (proposal number 2013091919). This work also utilized the Janus supercomputer, which is supported by the National Science Foundation (award number CNS-0821794), the University of Colorado Boulder, the University of Colorado Denver, and the National Center for Atmospheric Research. The Janus supercomputer is operated by the University of Colorado Boulder. This work additionally used the DiRAC Data Centric system at Durham University, operated by the Institute for Computational Cosmology on behalf of the STFC DiRAC HPC Facility (www.dirac.ac.uk). This equipment was funded by BIS National E-infrastructure capital grant ST/K00042X/1, STFC capital grants ST/H008519/1 and ST/K00087X/1, STFC DiRAC Operations grant ST/K003267/1 and Durham University. DiRAC is part of the National E-Infrastructure. The research was supported in part by the European Research Council under the European Union's Seventh Framework Programme (FP7/2007-2013) ERC Grant agreement 278594-GasAroundGalaxies. Support was also provided by the Interuniversity Attraction Poles Programme initiated by the Belgian Science Policy Office ([AP P7/08 CHARM]), as well as the consolidated grant from the STFC (ST/L00075X/1). RAC is a Royal Society University Research Fellow. AJR is supported by the Lindheimer Fellowship at Northwestern University. A database with many of the galaxy properties in EAGLE is publicly available and described in McAlpine et al. (2016).

REFERENCES

Aguirre A., Hernquist L., Schaye J., Weinberg D. H., Katz N., Gardner J., 2001, ApJ, 560, 599
Baes M., Verstappen J., De Looze I., Fritz J., Saftly W., Vidal Pérez E., Stalevski M., Valcke S., 2011, ApJS, 196, 22
Bahé Y. M. et al., 2016, MNRAS, 456, 1115
Bauer A. E. et al., 2013, MNRAS, 434, 209
Behroozi P. S., Wechsler R. H., Conroy C., 2013, ApJ, 770, 57
Booth C. M., Schaye J., 2009, MNRAS, 398, 53
Bordoloi R. et al., 2011, ApJ, 743, 10
Bordoloi R. et al., 2014, ApJ, 796, 136
Borthakur S., Heckman T., Strickland D., Wild V., Schiminovich D., 2013, ApJ, 768, 18
Borthakur S. et al., 2015, ApJ, 813, 46
Bouché N., Lehnert M. D., Aguirre A., Péroux C., Bergeron J., 2007, MNRAS, 378, 525
Bouché N., Hohensee W., Vargas R., Kacprzak G. G., Martin C. L., Cooke J., Churchill C. W., 2012, MNRAS, 426, 801
Bower R. G., Benson A. J., Malbon R., Helly J. C., Frenk C. S., Baugh C. M., Cole S., Lacey C. G., 2006, MNRAS, 370, 645
Camps P., Baes M., 2015, Astron. Comput., 9, 20
Cen R., Chisari N. E., 2011, ApJ, 731, 11
Cen R., Fang T., 2006, ApJ, 650, 573
Chabrier G., 2003, PASP, 115, 763
Chang Y.-Y., van der Wel A., da Cunha E., Rix H.-W., 2015, ApJS, 219, 8
Chen H.-W., Helsby J. E., Gauthier J.-R., Shectman S. A., Thompson I. B., Tinker J. L., 2010, ApJ, 714, 1521
Chisholm J., Tremonti C. A., Leitherer C., Chen Y., Wofford A., Lundgren B., 2015, ApJ, 811, 149
Churchill C. W., Trujillo-Gomez S., Nielsen N. M., Kacprzak G. G., 2013, ApJ, 779, 87
Crain R. A., McCarthy I. G., Frenk C. S., Theuns T., Schaye J., 2010, MNRAS, 407, 1403
Crain R. A., McCarthy I. G., Schaye J., Theuns T., Frenk C. S., 2013, MNRAS, 432, 3005
Crain R. A. et al., 2015, MNRAS, 450, 1937
Creasey P., Theuns T., Bower R. G., Lacey C. G., 2011, MNRAS, 415, 3706
Cullen L., Dehnen W., 2010, MNRAS, 408, 669
Dalla Vecchia C., Schaye J., 2012, MNRAS, 426, 140
Danforth C. W. et al., 2016, ApJ, 817, 111
Davé R., Oppenheimer B. D., 2007, MNRAS, 374, 427
Dehnen W., Aly H., 2012, MNRAS, 425, 1068
Dekel A. et al., 2009, Nature, 457, 451
Dolag K., Borgani S., Murante G., Springel V., 2009, MNRAS, 399, 497
Durier F., Dalla Vecchia C., 2012, MNRAS, 419, 465
Faerman Y., Sternberg A., McKee C. F., 2016, ApJ, submitted (arXiv:1602.00689)
Ferland G. J., Korista K. T., Verner D. A., Ferguson J. W., Kingdon J. B., Verner E. M., 1998, PASP, 110, 761
Ford A. B., Oppenheimer B. D., Davé R., Katz N., Kollmeier J. A., Weinberg D. H., 2013, MNRAS, 432, 89
Ford A. B., Davé R., Oppenheimer B. D., Katz N., Kollmeier J. A., Thompson R., Weinberg D. H., 2014, MNRAS, 444, 1260
Ford A. B. et al., 2016, MNRAS, 459, 1745
Furlong M. et al., 2015a, MNRAS, 450, 4486
Furlong M. et al., 2015b, preprint (arXiv:1510.05645)
Gallazzi A., Charlot S., Brinchmann J., White S. D. M., Tremonti C. A., 2005, MNRAS, 362, 41
Gilbank D. G., Baldry I. K., Balogh M. L., Glazebrook K., Bower R. G., 2010, MNRAS, 405, 2594
Gnat O., Ferland G., 2012, ApJS, 199, 20
Guo Q. et al., 2011, MNRAS, 413, 101
Gutcke T. A., Stinson G. S., Macciò A. V., Wang L., Dutton A. A., 2016, MNRAS, submitted (arXiv:1602.06956)
Haardt F., Madau P., 2001, in Neumann D. M., Van J. T. T., eds, XXXVIth Rencontres de Moriond, Clusters of Galaxies and the High Redshift

Universe Observed in X-rays: Recent Results of XMM–Newton and Chandra. CEA, Saclay
Heckman T. M., Norman C. A., Strickland D. K., Sembach K. R., 2002, ApJ, 577, 691
Henriques B. M. B., White S. D. M., Thomas P. A., Angulo R., Guo Q., Lemson G., Springel V., Overzier R., 2015, MNRAS, 451, 2663
Hopkins P. F., 2013, MNRAS, 428, 2840
Hummels C. B., Bryan G. L., Smith B. D., Turk M. J., 2013, MNRAS, 430, 1548
Hutchings R. M., Thomas P. A., 2000, MNRAS, 319, 721
Jenkins A., 2010, MNRAS, 403, 1859
Jenkins A., Booth S., 2013, preprint (arXiv:1306.5771)
Kacprzak G. G., Churchill C. W., Evans J. L., Murphy M. T., Steidel C. C., 2011, MNRAS, 416, 3118
Kacprzak G. G., Muzahid S., Churchill C. W., Nielsen N. M., Charlton J. C., 2015, ApJ, 815, 22
Kennicutt R. C., 1998, ApJ, 498, 541
Kereš D., Katz N., Weinberg D. H., Davé R., 2005, MNRAS, 363, 2
Lagos C. d. P. et al., 2015, MNRAS, 452, 3815
Lagos C. d. P. et al., 2016, MNRAS, 459, 2632
Leitner S. N., 2012, ApJ, 745, 149
Liang C. J., Chen H.-W., 2014, MNRAS, 445, 2061
McAlpine S. et al., 2016, Astron. Comput., 15, 72
Martin C. L., Shapley A. E., Coil A. L., Kornei K. A., Bundy K., Weiner B. J., Noeske K. G., Schiminovich D., 2012, ApJ, 760, 127
Moster B. P., Naab T., White S. D. M., 2013, MNRAS, 428, 3121
Nielsen N. M., Churchill C. W., Kacprzak G. G., 2013, ApJ, 776, 115
Nielsen N. M., Churchill C. W., Kacprzak G. G., Murphy M. T., Evans J. L., 2015, ApJ, 812, 83
Oppenheimer B. D., Davé R. A., 2006, MNRAS, 373, 1265
Oppenheimer B. D., Davé R. A., 2009, MNRAS, 395, 1875
Oppenheimer B. D., Schaye J., 2013a, MNRAS, 434, 1043 (OS13)
Oppenheimer B. D., Schaye J., 2013b, MNRAS, 434, 1063
Oppenheimer B. D., Davé R., Kereš D., Fardal M., Katz N., Kollmeier J., Weinberg D. H., 2010, MNRAS, 406, 2325
Oppenheimer B. D., Davé R., Katz N., Kollmeier J. A., Weinberg D. H., 2012, MNRAS, 420, 829
Peeples M. S., Werk J. K., Tumlinson J., Oppenheimer B. D., Prochaska J. X., Katz N., Weinberg D. H., 2014, ApJ, 786, 54 (P14)
Planck Collaboration I, 2014, A&A, 571, A1
Price D. J., 2008, J. Comput. Phys., 227, 10040
Rahmati A., Schaye J., Bower R. G., Crain R. A., Furlong M., Schaller M., Theuns T., 2015, MNRAS, 452, 2034
Rahmati A., Schaye J., Crain R. A., Oppenheimer B. D., Schaller M., Theuns T., 2016, MNRAS, 459, 310
Richings A. J., Schaye J., 2016, MNRAS, preprint (arXiv:1604.01035)
Richings A. J., Schaye J., Oppenheimer B. D., 2014, MNRAS, 440, 3349
Rosas-Guevara Y. M. et al., 2015, MNRAS, 454, 1038
Rubin K. H. R., Prochaska J. X., Koo D. C., Phillips A. C., Martin C. L., Winstrom L. O., 2014, ApJ, 794, 156
Rudie G. C. et al., 2012, ApJ, 750, 67
Salpeter E. E., 1955, ApJ, 121, 161
Savage B. D. et al., 2010, ApJ, 719, 1526
Schaller M., Dalla Vecchia C., Schaye J., Bower R. G., Theuns T., Crain R. A., Furlong M., McCarthy I. G., 2015, MNRAS, 454, 2277
Schaye J., 2004, ApJ, 609, 667
Schaye J., Dalla Vecchia C., 2008, MNRAS, 383, 1210
Schaye J., Aguirre A., Kim T.-S., Theuns T., Rauch M., Sargent W. L. W., 2003, ApJ, 596, 768
Schaye J. et al., 2015, MNRAS, 446, 521 (S15)
Segers M. C., Crain R. A., Schaye J., Bower R. G., Furlong M., Schaller M., Theuns T., 2016, MNRAS, 456, 1235
Shen S., Madau P., Conroy C., Governato F., Mayer L., 2014, ApJ, 792, 99
Shull J. M., 2014, ApJ, 784, 142
Shull J. M., Smith B. D., Danforth C. W., 2012, ApJ, 759, 23
Smith B. D., Hallman E. J., Shull J. M., O'Shea B. W., 2011, ApJ, 731, 6
Springel V., 2005, MNRAS, 364, 1105
Springel V., Hernquist L., 2003a, MNRAS, 339, 289
Springel V., Hernquist L., 2003b, MNRAS, 339, 312
Springel V., White S. D. M., Tormen G., Kauffmann G., 2001, MNRAS, 328, 726
Stinson G. S. et al., 2012, MNRAS, 425, 1270
Stocke J. T., Keeney B. A., Danforth C. W., Shull J. M., Froning C. S., Green J. C., Penton S. V., Savage B. D., 2013, ApJ, 763, 148
Suresh J., Bird S., Vogelsberger M., Genel S., Torrey P., Sijacki D., Springel V., Hernquist L., 2015a, MNRAS, 448, 895
Suresh J., Rubin K. H. R., Kannan R., Werk J. K., Hernquist L., Vogelsberger M., 2015b, MNRAS, submitted (arXiv:1511.00687)
Tepper-Garcia T., Richter P., Schaye J., Booth C. M., Dalla Vecchia C., Theuns T., Wiersma R. P. C., 2011, MNRAS, 413, 190
Tescari E., Viel M., D'Odorico V., Cristiani S., Calura F., Borgani S., Tornatore L., 2011, MNRAS, 411, 826
Thom C., Chen H.-W., 2008, ApJS, 179, 37
Tilton E. M., Danforth C. W., Shull J. M., Ross T. L., 2012, ApJ, 759, 112
Tornatore L., Borgani S., Viel M., Springel V., 2010, MNRAS, 402, 1911
Trayford J. W. et al., 2015, MNRAS, 452, 2879
Tremonti C. A. et al., 2004, ApJ, 613, 898
Tripp T. M., Semback K. R., Bowen D. V., Savage B. D., Jenkins E. B., Lehner N., Richter P., 2008, ApJS, 177, 39
Tumlinson J. et al., 2011, Science, 334, 948 (T11)
Tumlinson J. et al., 2013, ApJ, 777, 59
Turner M. L., Schaye J., Steidel C. C., Rudie G. C., Strom A. L., 2014, MNRAS, 445, 794
van de Voort F., Schaye J., Altay G., Theuns T., 2012, MNRAS, 421, 2809
Vasiliev E. O., Ryabova M. V., Shchekinov Y. A., 2015, MNRAS, 446, 3078
Wakker B. P., Savage B. D., 2009, ApJS, 182, 378
Wendland H., 1995, Adv. Comput. Math., 4, 389
Werk J. K., Prochaska J. X., Thom C., Tumlinson J., Tripp T. M., O'Meara J. M., Meiring J. D., 2012, ApJS, 198, 3
White S. D. M., 1994, preprint (arXiv:astro-ph/9410043)
Wiersma R. P. C., Schaye J., Smith B. D., 2009a, MNRAS, 393, 99
Wiersma R. P. C., Schaye J., Theuns T., Dalla Vecchia C., Tornatore L., 2009b, MNRAS, 399, 574
Wiersma R. P. C., Schaye J., Dalla Vecchia C., Booth C. M., Theuns T., Aguirre A., 2010, MNRAS, 409, 132
Yoshikawa K., Sasaki S., 2006, PASJ, 58, 641
Zahid H. J., Dima G. I., Kewley L. J., Erb D. K., Davé R., 2012, ApJ, 757, 54
Zahid H. J., Dima G. I., Kudritzki R.-P., Kewley L. J., Geller M. J., Hwang H. S., Silverman J. D., Kashino D., 2014, ApJ, 791, 130

APPENDIX A: NON-EQUILIBRIUM EFFECTS

NEQ effects are generally small when considering circumgalactic O VI within 150 kpc exposed to a slowly evolving ionization background such as that specified by Haardt & Madau (2001). Fig. A1 shows the O VI column density in the equilibrium runs (cyan) and the NEQ runs (grey) at $z = 0.205$. The bottom panel shows that the differences are small – equilibrium zooms have +0.01 and +0.02 dex greater columns than NEQ zooms for L^* and group haloes, respectively. Column densities of high oxygen ions (O VI and above) typically differ by less than 30 per cent (0.1 dex) along individual lines of sight. The scatter is larger for group haloes with smaller O VI columns, where an episodic fluctuation can make a larger difference. Galaxy properties (M^* and sSFR) are indistinguishable between the two sets of simulations.

Our results appear to agree with Cen & Fang (2006) and Yoshikawa & Sasaki (2006), who find that NEQ effects matter for O VI mainly in the low-density, diffuse IGM where collisional ionization timescales become long compared to the timescales on which gas is shocked. One caveat is that we may underestimate the NEQ effects, because SPH smooths out shocks (Hutchings &

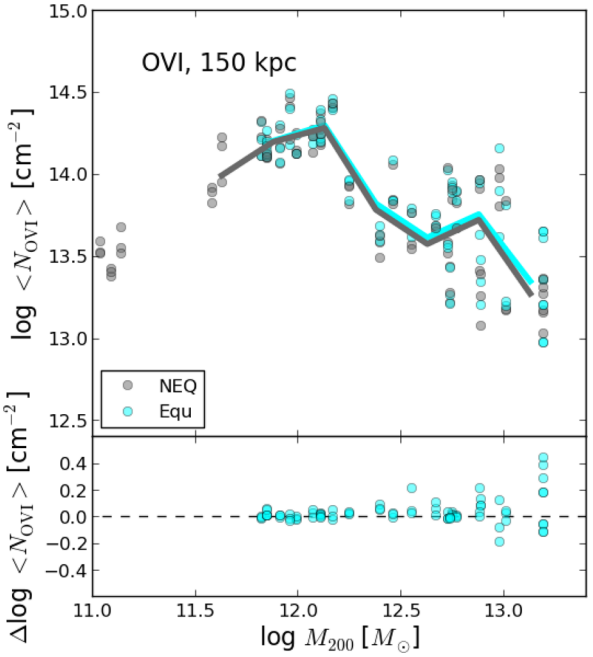

Figure A1. O VI aperture column densities within 150 kpc for our standard NEQ runs at $z = 0.205$ (grey, a repeat of the left-hand panel of Fig. 4), and runs with equilibrium ionization and cooling (cyan) with the differences relative to the standard NEQ runs shown on the bottom panel (for each halo there are three circles corresponding to three projections). Thick lines of the same colour in the top panel are binned averages. The runs diverge at $z = 0.503$ for L^* haloes and $z = 0.282$ for all but one group halo when the NEQ module is activated for the NEQ runs. Except for some high-mass haloes, the differences are small.

Thomas 2000; Creasey et al. 2011). Our simulations find that NEQ ionization and cooling under a slowly evolving ionization background such as Haardt & Madau (2001) do not significantly alter the O VI CGM statistics, and will further explore NEQ effects in such simulations in a future paper. However, a fluctuating local source of radiation, as expected for AGN, will introduce significant NEQ effects (Oppenheimer & Schaye 2013b).

APPENDIX B: RESOLUTION TESTS AND COMPARISONS WITH LARGE VOLUMES

We compare our results to higher and lower resolution simulations, using both our zooms and other periodic EAGLE runs. We consider stellar masses relative to abundance matching constraints in Fig. B1 and 150 kpc aperture O VI column densities in Fig. B2.

B1 Metal smoothing at the same resolution

We first compare matched haloes at the same resolution in the *M5.3* L^* zooms (grey) and in RECAL-L025N0752 (yellow, the difference with the grey circles indicated in the bottom panel). This comparison tests the effect of SPH-smoothing of elemental abundances, which is done in RECAL-L025N0752 but not in the zooms as discussed in Section 2.3.3. The other differences between these two runs are NEQ versus equilibrium, which was covered in Appendix A and is insignificant for M_* and $\langle N_{\rm O\,VI}\rangle_{150}$, as well as the zoom method. We find 0.15 dex higher stellar masses for L^* galaxies in RECAL-L025N0752, which closely matches the 0.11 dex higher stellar masses we find in five *M5.3* smoothed-metallicity zooms. The O VI columns are essentially unchanged, being 0.03 dex

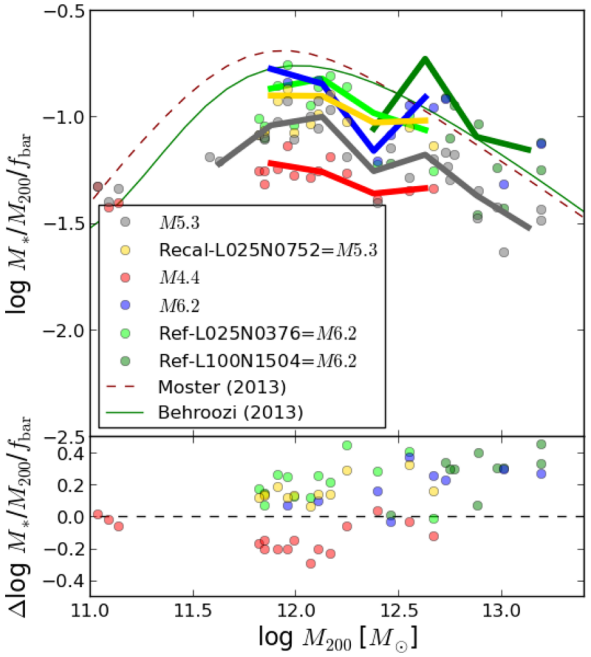

Figure B1. Galaxy formation efficiency as a function of halo mass for our standard NEQ runs at $z = 0.205$ (in grey) and for matched haloes in RECAL-L025N0752 (yellow) at the same resolution (*M5.3*), the higher resolution *M4.4* zooms (red), and the lower resolution *M6.2* zooms (blue). We also compare to the matched haloes in REF-L025N0376 (green) and REF-L100N1504 (dark green). The outputs for EAGLE volumes are at $z = 0.187$, and the abundance matching constraints from Behroozi et al. (2013, solid green) and Moster et al. (2013, dashed red) are at $z = 0.2$. The top panel shows the absolute values (circles) and binned averages (thick lines), and the bottom panel shows differences relative to the *M5.3* zooms (grey circles in top panel).

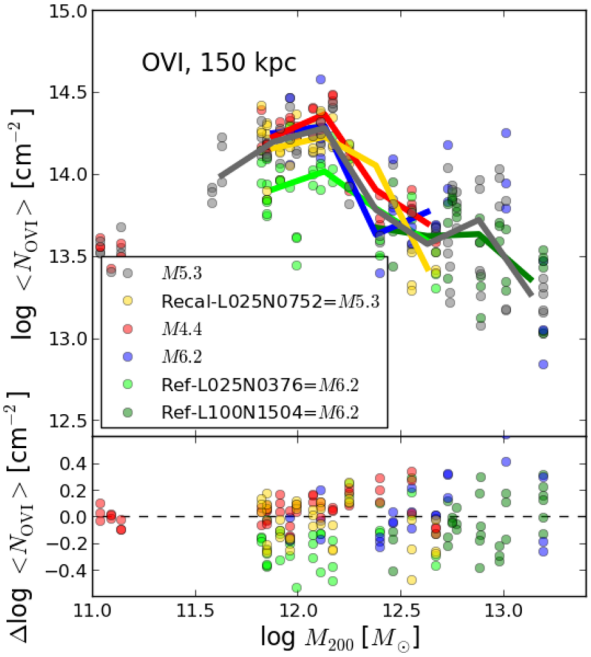

Figure B2. O VI aperture column densities within 150 kpc for our standard NEQ runs at $z = 0.205$ for the same runs as shown in Fig. B1, showing a range of 64 (4) in mass (spatial) resolution. The aperture is centred on the galaxy coordinates given in each respective simulation (zoom and EAGLE volume). The top panel shows the absolute values (circles) and binned averages (thick lines), and the bottom panel shows differences relative to the *M5.3* zooms (grey circles in top panel).

Table B1. *M4.4* and *M6.2* zoom simulation runs.

Name	Resolution	log M_{200} ($M_\odot$)	m_{SPH} ($M_\odot$)	m_{DM1} ($M_\odot$)	ϵ (pc)	log M_* ($M_\odot$)	SFR ($M_\odot$ yr^{-1})	z_{NEQ}	z_{low}
Gal001	*M4.4*	12.07	2.77e+04	1.49e+05	175	9.98	1.166	0.503	0.0
Gal002	*M4.4*	12.27	2.85e+04	1.53e+05	175	10.20	1.538	0.503	0.0
Gal003	*M4.4*	12.11	2.80e+04	1.50e+05	175	10.05	1.311	0.503	0.0
Gal004	*M4.4*	12.01	2.83e+04	1.52e+05	175	9.93	1.077	0.503	0.0
Gal005	*M4.4*	12.16	2.84e+04	1.53e+05	175	10.17	1.323	0.503	0.099
Gal006	*M4.4*	11.93	2.77e+04	1.49e+05	175	9.88	0.620	0.503	0.0
Gal007	*M4.4*	11.82	2.83e+04	1.52e+05	175	9.76	0.953	0.503	0.0
Gal008	*M4.4*	11.87	2.83e+04	1.52+05	175	9.75	0.647	0.503	0.205
Gal009	*M4.4*	11.85	2.83e+04	1.52e+05	175	9.79	0.772	0.503	0.205
Gal010[a]	*M4.4*	12.69	2.83e+04	1.52e+05	175	10.55	2.019	–	–
Gal010[a]	*M6.2*	12.69	1.86e+06	9.98e+06	700	10.93	4.677	–	–
Grp003[a]	*M6.2*	12.71	1.90e+06	1.02e+07	700	10.99	0.708	–	–
Grp006[a]	*M6.2*	12.99	1.78e+06	9.52e+06	700	10.87	0.000	–	–
Grp008[a]	*M6.2*	13.15	1.85e+06	9.92+06	700	11.22	0.000	–	–

[a]These haloes were not run in NEQ.

lower in RECAL-L025N0752. Hence, metal smoothing slightly increases stellar masses but barely alters O VI CGM columns. This test also shows that our zooms do not statistically deviate from their parent simulations, so that our zoom results also hold for the EAGLE volumes. Therefore, we can compare our results directly to Rahmati et al. (2016) for global IGM metal statistics when they use RECAL-L025N0752.

B2 Resolution tests

We have run all *M5.3* zooms from the RECAL-L025N0752 box at *M4.4* resolution using the same parameters (RECAL prescription and particle-metallicities; red), which we show in both Figs B1 and B2. These runs, listed in Table B1, constitute a strong convergence test (S15), and better agreement is potentially achievable with recalibrated parameters. Seven out of 10 *M4.4* zooms are run in NEQ from $z = 0.503$ to at least $z = 0.205$, but the NEQ results are nearly identical to the equilibrium one. The large Gal010 zoom was run in equilibrium only, and provides three individual $M_{200} = 10^{12.4}$–$10^{12.7}$ $M_\odot$, $z = 0.205$ haloes to test if the decline in O VI above L^* persists at this higher resolution. We also ran a set of *M6.2* zooms using RECAL and particle metallicities (blue) for nine galaxies in four zooms, also listed in Table B1.

For L^* haloes, the *M4.4* zooms have 0.06 dex higher O VI columns despite having 0.18 dex lower stellar masses as mentioned in Section 6.1. This means that a greater proportion of the oxygen formed in higher resolution simulations (since oxygen production $\propto M_*$) appears as O VI within 150 kpc of the galaxy. The decline of O VI above $M_{200} > 10^{12.3}$ $M_\odot$ however is robust with the three Gal010 haloes ($M_{200} = 10^{12.42}$, $10^{12.58}$, and $10^{12.69}$ $M_\odot$) showing a considerable decline in O VI columns relative to L^* masses. These three haloes have O VI columns averaging $10^{13.79}$ cm^{-2}, which is 3 × lower than the *M4.4* L^* columns – $10^{14.31}$ cm^{-2}, and the same decline as seen in the *M5.3* zooms. Hence, the conclusion that O VI traces the virial temperature of L^* haloes and therefore declines at higher masses is corroborated by these 8 × better mass resolution simulations. Nevertheless, the *M4.4* zooms underpredict abundance matching constraints by a factor of ∼3, which implies that the stellar feedback indeed needs to be recalibrated at *M4.4* resolution to inject less energy in order to create galaxies of the same stellar mass in the L^* mass range. This is likely a consequence of improved numerical efficiency of our stochastic thermal feedback implemented at the higher resolution.

The *M6.2* zooms are the only galaxies run at this resolution using the RECAL prescription, because L100N1504 uses the REF parameter values. In the L^* range, galaxy stellar masses are on average 0.09 dex higher than *M5.3* while the O VI columns are 0.06 dex lower. This continues the trend seen with the *M4.4* zooms of a greater proportion of oxygen produced by stars showing up as O VI within 150 kpc at higher resolution. The decline in O VI above $M_{200} = 10^{12.3}$ $M_\odot$ persists at *M6.2* resolution. This trend is robust at all three resolutions, indicating a decline by a factor of $\gtrsim$3 in O VI columns from L^* to group haloes. The resolution convergence is better for $\langle N_{O\,VI}\rangle_{150}$ values than for M_* across a factor of 64 in mass resolution; however, it should be noted that oxygen production is nearly linear with stellar mass, so that the over-riding trend is a greater fraction of oxygen produced at higher resolution becomes CGM O VI within 150 kpc.

B3 Comparison to EAGLE volumes

In the previous section, we compared our results in the 'strong convergence' regime, defined by S15 as not changing the subgrid models across different resolutions, using the RECAL prescription. However, to compare to the main EAGLE simulations that use the 'REF' model at *M6.2* resolution, we cross-reference the L^* ($10^{11.7}$–$10^{12.3}$ $M_\odot$) haloes at *M5.3* resolution to REF-L025N0376 (green in Figs B1 and B2) and the group ($10^{12.7}$–$10^{13.3}$ $M_\odot$) haloes to REF-L100N1504 (dark green) to perform a test of 'weak convergence' where the subgrid models are changed. This allows us to verify our higher resolution zoom results to the much larger sample from the EAGLE volumes, which are used throughout many EAGLE papers including Rahmati et al. (2016).

Relative to our *M5.3* zooms, the REF model has L^* (group) stellar masses that are 0.21 (0.31) dex higher, while O VI columns are 0.24 (0.06) dex lower. The REF model better matches the abundance matching constraints (by design), while our zooms have the additional difference of using particle rather than smoothed-SPH metallicities on top of the weak convergence comparison of the standard REF and RECAL prescriptions. The decline from L^* to group haloes for $\log[\langle N_{O\,VI}\rangle_{150}/\mathrm{cm}^{-2}]$ is smaller (13.96–13.56) than in the matched *M5.3* zooms (14.20–13.62), but still significant.

To generalize these statistics to all haloes in the EAGLE REF volumes, we find the average $\log[\langle N_{O\,VI}\rangle_{150}/\mathrm{cm}^{-3}]$ in L^* (group) haloes using REF-L025N0376 (REF-L100N504) of (13.83) 13.61, where each sample contains at least 50 haloes. While the decline is still apparent,

it is smaller at the REF resolution. We also used the intermediate-sized REF-L050N0752 box to find 13.83 (13.66) for 294 (52) L^* (group) haloes. However, it must be noted that this sample includes *all* the haloes in 0.6 dex M_{200} bins, which biases each bin to be dominated by haloes at the lower mass end of the bin (where there are more haloes) as opposed to the zooms chosen to more evenly sample the masses within these bins. Indeed, making the M_{200} bins smaller (0.3 dex wide) in REF-L050N0752, leads to a slightly greater decline from 13.89 to 13.61.

The L^* O VI columns are considerably smaller at REF resolution, which is again apparent when we look at all L^* haloes in RECAL-L025N0752 finding $\langle N_{\rm O\,VI}\rangle_{150} = 10^{14.09}\,{\rm cm}^{-2}$, which is 0.26 dex higher than for REF-L025N0376. This supports the findings of Rahmati et al. (2016) where significantly more high O VI columns ($>10^{14}\,{\rm cm}^{-2}$) occur in RECAL-L025N0752 than in the REF lower resolution simulations. While group halo O VI columns appear to not change much in the weak convergence limit, the O VI columns in L^* haloes are significantly higher in the RECAL simulations, which affects both COS-Halos type observations and global IGM observations (Rahmati et al. 2016).

NoAGN simulations. Finally, we consider the NoAGN-L050N0752 run (*M6.2* resolution), and find $\log[\langle N_{\rm O\,VI}\rangle_{150}/{\rm cm}^{-2}] = 13.96$ (13.58) for L^* (group) haloes, which compares to 13.83 (13.66) in REF-L050N0752. Thus, the conclusion that AGN are not responsible for the reduction of O VI columns with mass as discussed in Section 6.2, holds also for this larger sample of group haloes, and the difference in O VI column density is actually *stronger* in the absence of AGN. Globally, there exists more O VI in the NoAGN models (Rahmati et al. 2016), which likely owes to L^* haloes hosting more O VI while group haloes harbour less O VI within 150 kpc despite forming twice as many stars.

This paper has been typeset from a TEX/LATEX file prepared by the author.